Journal Pre-proof

Exploration of carbamide derived pyrimidine-thioindole conjugates as potential VEGFR-2 inhibitors with anti-angiogenesis effect

Sravani Sana, Velma Ganga Reddy, Sonal Bhandari, T. Srinivasa Reddy, Ramya Tokala, Akash P. Sakla, Suresh K. Bhargava, Nagula Shankaraiah

PII: S0223-5234(20)30428-1

DOI: https://doi.org/10.1016/j.ejmech.2020.112457

Reference: EJMECH 112457

To appear in: *European Journal of Medicinal Chemistry*

Received Date: 12 March 2020

Revised Date: 28 April 2020

Accepted Date: 10 May 2020

Please cite this article as: S. Sana, V.G. Reddy, S. Bhandari, T.S. Reddy, R. Tokala, A.P. Sakla, S.K. Bhargava, N. Shankaraiah, Exploration of carbamide derived pyrimidine-thioindole conjugates as potential VEGFR-2 inhibitors with anti-angiogenesis effect, *European Journal of Medicinal Chemistry* (2020), doi: https://doi.org/10.1016/j.ejmech.2020.112457.

Graphical Abstract

Exploration of Carbamide Derived Pyrimidine-Thioindole Conjugates as Potential VEGFR-2 Inhibitors with Anti-Angiogenesis Effect

Sravani Sana[a], Velma Ganga Reddy[b]*, Sonal Bhandari[a], T. Srinivasa Reddy[b], Ramya Tokala[a], Akash P. Sakla[a], Suresh K. Bhargava[b], Nagula Shankaraiah[a]*

[a]*Department of Medicinal Chemistry, National Institute of Pharmaceutical Education and Research (NIPER), Hyderabad - 500 037, India*

[b]*Centre for Advanced Materials & Industrial Chemistry (CAMIC), School of Science, RMIT University, GPO Box 2476, Melbourne 3001, Australia*

E-mail.: shankar.niperhyd@gov.in

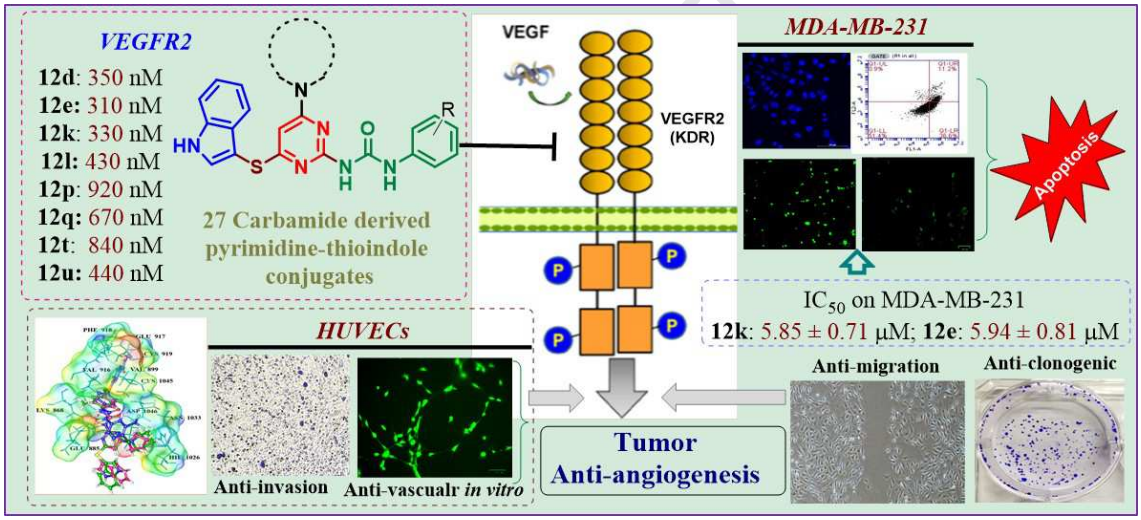

Exploration of Carbamide Derived Pyrimidine-Thioindole Conjugates as Potential VEGFR-2 Inhibitors with Anti-Angiogenesis Effect

Sravani Sana[a], Velma Ganga Reddy[b]*, Sonal Bhandari[a], T. Srinivasa Reddy[b], Ramya Tokala[a], Akash P. Sakla[a], Suresh K. Bhargava[b], Nagula Shankaraiah[a]*

[a]*Department of Medicinal Chemistry, National Institute of Pharmaceutical Education and Research (NIPER), Hyderabad - 500 037, India*

[b]*Centre for Advanced Materials & Industrial Chemistry (CAMIC), School of Science, RMIT University, GPO Box 2476, Melbourne 3001, Australia*

Abstract: The development of new small molecules from known structural motifs through molecular hybridization is one of the trends in drug discovery. In this connection, we have combined the two pharmacophoric units (pyrimidine and thioindole) in a single entity *via* molecular hybridization strategy along with introduction of urea functionality at C2 position of pyrimidine to increase the efficiency of H-bonding interactions. Among the synthesized conjugates **12a-aa**, compound **12k** was found to exhibit significant IC_{50} values 5.85, 7.87, 6.41 and 10.43 µM against MDA-MB-231 (breast), HepG2 (liver), A549 (lung) and PC-3 (prostate) cancer cell lines, respectively. All these compounds were further evaluated for their inhibitory activities against VEGFR-2 protein. The results specified that among the tested compounds, **12d**, **12e**, **12k**, **12l**, **12p**, **12q**, **12t** and **12u** prominently suppressed VEGFR-2, with IC_{50} values of 310 to 920 nM in association to the positive control (210 nM). Angiogenesis inhibition was evident by tube formation assay in HUVECs and cell-invasion by transwell assay. The mechanism of cellular toxicity on MDA-MB-231 was found through depolarisation of mitochondrial membrane potential, increased ROS production and subsequent DNA damage resulting in apoptosis induction. Moreover, clonogenic and wound healing assays designated the inhibition of colony formation and cell migration by **12k** in a dose-dependent manner. Molecular docking studies also shown that compound **12k** capably intermingled with catalytically active residues GLU-885, ASP-1046 of the VEGFR-2 through hydrogen-bonding interactions.

Keywords: Angiogenesis, VEGFR-2, pyrimidine-thioindole, urea, cytotoxicity, apoptosis.

Corresponding author: Dr. Nagula Shankaraiah, E-mail: shankar@niperhyd.ac.in; shankarnbs@gmail.com; Dr. Velma Ganga Reddy, E-mail: ganga.reddy.velma@rmit.edu.au.

1.0 Introduction

In drug discovery, lead generation always starts with the identification of chemical starting points with the consumption of known literature such as fast-follower or knowledge-based programs [1]. According to the scrutiny of Hit-to-Clinical Pairs stated in 2016-2017, a slight fewer than half (43%) of the clinical candidates defined were resulted from recognized starting points [2]. Among the 66 hit-to-clinical pairs, 30% of disease area was led by oncology, particularly targeting kinase receptors [3] highlighting cancer as a focus of interest for the expansion of new anticancer agents to overcome multidrug resisitance with restored clinical assistance [4].

Angiogenesis is a multitier strategy, wherein endothelial cells become stimulated, dissociate, migrate and proliferate to form new sprouts from the pre-existing blood vessels and observed to be pivotal during the embryo development, wound healing and reproduction [5]. Metastatic growth of primary tumors is an angiogenesis-dependent process, regulated by numerous stimulatory and inhibitory pathways, of which, growth factors such as VEGF, EGF, FGF, and PIGF have been identified as critical regulators [6]. Among these, Vascular Endothelial Growth Factor (VEGF) is a potent angiogenic tyrosine kinase receptor, overexpressed in majority of the solid tumors. VEGFR-2 is the prime mediator of VEGF-induced angiogenic signaling, which makes the target attract toward certain advanced cancers for involvement in the multitier strategies of angiogenesis, including vascular permeability, endothelial cell proliferation, migration, and survival [7]. Moreover, a significant number of small molecules of VEGFR-2 inhibitors namely sorafenib, sunitinib, axitinib (**A**, **Figure 1**), vatalanib and regorafenib have been approved for clinical use in cancer therapy. Taking these into consideration, targeting VEGFR-2 represents as a hopeful strategy for quantifiable benefit in the treatment of cancer [8].

Clinical success rate and presence of pyrimidine ring in DNA and RNA explicates its medicinal attributes and contemporary interest of researchers towards the development of potential therapeutic candidates in drug discovery [9]. Existence of pyrimidine in small molecule inhibitors as an essential fragment has been evidenced to hold diverse therapeutic aptitudes such as anticancer [10], anti-HIV, antidiabetic [11], antihypertensive, analgesic, antimicrobial, antiinflammatory [12], antitubercular, A2B adenosine receptor antagonists and antibacterial [13]. In addition, the tumor cell-killing potential of pyrimidine based frameworks has been witnessed

through diverse mechanisms, taking an account of inhibition of tyrosine kinase [14], serine/threonine protein kinase, histone deacetylase [15], autotaxin, heat shock protein, inositol kinase [16], etc. Pazopanib (**B**, **Figure 1**) is a pyrimidine centered small molecule identified with antiangiogenetic effect, approved by FDA in 2009 as multi-targeted receptor tyrosine kinase inhibitor [17]. Incessantly, CEP-11981 (**C**, **Figure 1**), a potent multi-targeted cytotoxic pyrimidine derivative was recognized with antiangiogenetic activity [18].

Besides, indole is a significant basis for biologically active compounds, which may possibly be acquired from organic synthesis or isolated from natural products. Indole as a core nucleus has been explored for various therapeutic activities such as anticancer [19], anti-inflammatory, antioxidant, anti-HIV [20], antimalarial, anti-tubercular, anticonvulsant, antidiabetic [21], antimicrobial, antifungal, antidyslipidemic and so on [22]. Cediranib (**D**, **Figure 1**) is an indole fused trioxyquinazoline derivative and observed to retain better discrimination over a panel of tyrosine and serine/threonine kinases along with VEGFR inhibitory activity. Brivanib (**E**, **Figure 1**) is also an indole based multi-targeted tyrosine kinase inhibitor with anti-tumorigenic effects towards hepatocellular carcinoma [23].

<Insert Figure 1 here>

As well, the evolution in the development of urea and its derivatives amplified the drug discovery since the latter half of the 20th century, exhibiting broad range of medicinal applications like anticancer, antibacterial, anticonvulsive, anti-HIV and anti-diabetic [24]. In precise, antitumor activity of urea functionality is emphasized by targeting protein kinase or microtubules with the ability of establishing multiple stable hydrogen bonds with protein and receptor targets by improving drug properties such as potency and selectivity [25]. Sorafenib (**F**, **Figure 1**) is a diaryl urea multikinase inhibitor approved in 2007 by FDA, underlining the significance of protein-ligand interaction with the formation of critical hydrogen-bonding with main-chain atoms of Asp1046 and the side-chain atoms of Glu885 vascular endothelial growth factor receptor 2 (VEGFR-2) [26]. In the recent years, considerable amount of aryl urea substructures has been introduced clinically, especially in the fields of kinase inhibitors i.e., regorafenib (**G**, **Figure 1**), linifanib and lenvatinib as VEGFR inhibitors [27], tandutinib as type III receptor tyrosine kinase inhibitor, gedatolisib as dual inhibitor of PI3K/mTOR [28].

Incorporation of molecular docking into the drug design, reveals that the binding site of VEGFR-2 has some common pharmacophoric features for most of the VEGFR-2 inhibitors i.e. i) typically a hetero aromatic ring binds to the hinge region, ii) hydrogen bond-rich region indicates where hydrogen donors or acceptors like urea or amide are favorable, iii) hydrophobic I & II regions, which can put up monocyclic or bicyclic ring structures [29]. Moreover, the association of molecular assortment that combines two or more pharmacophores in a single entity through molecular hybridization might be an effective way to aid the factors like synergism, drug resistance for better clinical upshot [30].

In the way of our obligation headed for the advance of bioactive molecules [31] and in sight of aforementioned distinctions regarding the pharmacophoric features and molecular hybridization by means of known VEGFR-2 inhibitors, a library of 600 molecules were designed and docked in to the active site of VEGR-2. Based on the results, a series of 27 carbamide derived pyrimidine-thioindole conjugates were synthesized based on the synthestic feasibility and predicted as encouraging molecules of VEGFR-2 inhibition. In the current work, all the defined molecules were armed with the crucial structural features like i) indole at C4 of pyrimidine as hinge-binding region, ii) urea functionality at C2 of pyrimidine as hydrogen-bond rich region, iii) 1˚/2˚ nitrogen-containing heterocycles at C6 of pyrimidine is designed to occupy hydrophobic I region, iv) pyrimidine ring is required to anchor hydrophobic II region.

<Insert Figure 2 here>

2.0 Results and Discussion

2.1 Chemistry

As depicted in **Scheme 1**, the carbamide derivatives of thioether-linked indole-pyrimidine conjugates **12a**–**aa** were synthesized in a merging slant utilizing the nucleophilic reactivity of thioindole substituted pyrimidin-2-amines **10a**–**i** with substituted aryl isocyanates **11a**–**f** as electrophiles. The key intermediate 1*H*-indole-3-thiol was synthesized by electrophilic attack of thiourea at C3-position of indole *via* alkaline treatment of thiourea intermediate. Next, a variety of 6-amino-pyrimidin-2-amines **9a**–**i** was synthesized according to the reported procedures [32]. The condensation reaction between diethyl malonate and guanidine hydrochloride in the presence of a base with elimination of ethanol leads to the formation of 2-aminopyrimidine-4,6-

diol. The alcoholic functionalities were then chlorinated using $POCl_3$ to form an easy leaving group i.e., chlorophosphite and subsequently chlorine group attacks the carbon of this intermediate to provide 4,6-dichloropyrimidin-2-amine. Next, one of the chlorine groups of 4,6-dichloropyrimidin-2-amine derivative undergoes nucleophilic substitution selectively with different 1˚ aromatic amines and cyclic 2˚ non-aromatic amines using acidic as well as basic conditions in protic solvents to afford 6-amino-pyrimidin-2-amines **9a**–**i**. The other chlorine was then substituted with indole-3-thiol as nucleophile using KI and Et_3N to afford 4-((1*H*-indol-3-yl)thio)-6-(1˚/2˚ amino)pyrimidin-2-amine **10a**–**i**. The nucleophilic amine group at C2 position of these derivatives was successively reacted with substituted aryl isocyanates to afford the titled carbamide derivatives of thioether-linked indole-pyrimidine conjugates **12a**–**aa**.

<Insert Scheme 1 here>

The most potent compound **12e** was characterized by ^{1}H NMR and showed a characteristic sharp singlet at δ 10.04 and 9.15 ppm which indicates the proton ensuing carbamide formation. Proton of –NH– corresponding to thioindole resonated as a singlet at δ 11.44 ppm. The doublet of one proton at δ 7.37 ppm belongs to the –CH– proton adjacent to the thioindole –NH. The signal at δ 6.06 ppm resembles the proton of –CH– at C5 position of pyrimidine. The multiplet of six protons at δ 1.44 and 1.58 ppm corresponds to $–CH_2–$ protons of C3, C5 and C4 protons of piperidine ring, respectively. The four protons of $–CH_2–$ at C2 and C6 which is adjacent to N–atom of piperidine ring resonated as a multiplet at δ 3.43 ppm. Distinctive methyl protons of phenyl urea seemed as a singlet at δ 1.89 ppm and the left over protons lie in the aromatic region at δ 7.68–6.96 ppm. Likewise, ^{13}C NMR interpretation of compound **12e** indicates the presence of carbonyl carbon of urea functionality at δ 152.7 ppm. The carbon in between the thioether bridge and N-1 atom of pyrimidine was resonated at δ 169.1 ppm. The C4-carbon of pyrimidine ring attached to the piperidine was appeared at δ 161.3 ppm. The C2-carbon of pyrimidine ring showed a characteristic peak at δ 157.4 ppm and all the remaining aromatic carbons resonate~~s~~ between δ 136.8–91.3 ppm. Distinctive methyl carbons of phenyl urea were resonated at δ 18.3 ppm. The signals at δ 24.4 and 25.5 ppm accounts for the C3, C–5 and C4 carbons of piperidine ring respectively. The two carbons of piperidine ring adjacent to N-atom resonated at δ 45.0 ppm. Similarly, all the synthesized derivatives were scrutinized by using HRMS, ^{1}H, ^{13}C NMR and FT-IR and are in agreement with the relevant structures as showed in the experimental

section. The HRMS (ESI) of all the compounds showed an $[M + H]^+$ or $[M + 2]^+$ peaks conforming their particular molecular formula.

2.2 Biological evaluation

2.2.1 *In vitro* anticancer screening

The synthesized pyrimidine-thioindole conjugates **12a**–**aa** were assessed for their *in vitro* cytotoxicity employing 3-(4,5-dimethylthiazol-2-yl)-2,5-diphenyltetrazolium bromide (MTT) assay [33] against certain human cancer cell lines like A549 (human lung cancer), PC-3 (human prostate cancer), MDA-MB-231(human breast cancer) and HepG2 (human liver cancer). The IC_{50} (μM) values from the *in vitro* anticancer screening of the derivatives **12a**–**aa** along with standard drug sorafenib were inferred in **Table 1**. Interestingly, the verified derivatives exhibited moderate to significant antiproliferative activity against the selected cancer cell lines. Remarkably, primary results directed that most of the synthesized derivatives **12a**–**aa** showed significant cytotoxicity against triple-negative breast cancer (TNBC) cell line such as MDA-MB-231. For instance, compounds **12b**–**i**, **12k**, **12l**, **12q**, **12t**, **12v**, **12z** and **12aa** exhibited notable antiproliferative activities with IC_{50} values 5.85 to 10.26 μM. Moreover, compounds also displayed good to moderate antiproliferative activities against A549 (lung) and PC-3 (prostate) cancer cell lines with IC_{50} values 6.41 to 48.43 μM and above.

From the detailed study of IC_{50} values, it was inferred that the derivatives holding five-membered nitrogen heterocyclic ring such as pyrrolidine influenced the activity on all tested cancer cell lines. Note worthily, one of the tested compounds **12k** of carbamide derivatives disclosed effective *in vitro* cytotoxicity against MDA-MB-231 breast cancer cell with IC_{50} value 5.85 μM. This derivative also observed to be active with corresponding IC_{50} values 6.41 μM, 7.87 μM and 10.42 μM against lung (A549), liver (HepG2) and prostate (PC-3). It was also observed that compound **12l** exposed to be active in liver (HepG2), lung (A549), breast (MDA-MB-231), and prostate (PC-3) with 50% inhibition at 7.15 μM, 8.93 μM, 9.44 μM and 12.86 μM respectively. It is obvious from IC_{50} values that the presence of thioindole attached to C4-pyrimidine ring was well tolerated for cytotoxicity. Nonetheless, it could be witnessed from the *in vitro* cytotoxicity results that the presence of non-aromatic nitrogen heterocycles significantly inclined the cytotoxic profile especially towards MDA-MB-231 breast cancer cell line which assumes that these results may support in identification of new anti-breast cancer agents with superior activity. Based on the cytotoxicity, the most potent compounds **12e** and **12k** were

selected for additional studies in the direction of identification of mechanism for cancer cell growth inhibition. Furthermore, all the titled compounds were screened for their VEGFR-2 inhibitory potency to realize the concealed mechanism of the anticancer effects.

<Insert Table 1 here>

2.3 *In-vitro* VEGFR-2 inhibition assay

VEGFR-2 inhibitory potency of indole-pyrimidine conjugates were tested for their *in vitro* activities with the inclusion of sorafenib (VEGFR-2 inhibitor) as a known positive control. The results were outlined in **Table 2**. In accordance with the obtained results, all the compounds exhibited from moderate (2.14 - 5.22 μM) to strong (0.31 - 1.92 μM) inhibitory activities when compared with sorafenib (210 nM). In specific, among the 27 molecules, 8 compounds potently inhibited VEGFR-2 with IC_{50} value of **12d** (IC_{50} = 350 nM), **12e** (IC_{50} = 310 nM), **12k** (IC_{50} = 330 nM), **12l** (IC_{50} = 430 nM), **12p** (IC_{50} = 920 nM), **12q** (IC_{50} = 670 nM), **12t** (IC_{50} = 840 nM) and **12u** (IC_{50} = 440 nM). Also, 9 compounds **12a**, **12b**, **12c**, **12f**, **12g**, **12n**, **12w**, **12z**, **12aa** exhibited good VEGFR-2 inhibitory activity at low micromolar IC_{50} values (1.13 to 1.92 μM). However, the other 10 compounds exhibited moderate inhibition to VEGFR-2 (2.14 to 5.22 μM).

<Insert Table 2 here>

3.0 *In silico* Studies

3.1 Molecular Docking

The higher inhibition pattern displayed by the title carbamide derivatives stimulated us to explore their feasible binding modes within VEGFR-2 kinase domain using molecular docking study, so that to afford an agreeable clarification for the consistency of biological activity. For this protocol, we selected PDB ID: 3WZE [34] cocrystallized with sorafenib and then the authentication of the docking procedure was achieved by re-docking of the co-crystallized ligand (sorafenib) in the VEGFR-2 active site, in which sorafenib reproduced all the key interactions with critical amino acids in the active site (Cys919, Glu885, and Asp1046). This point outs the aptness of the used protocol for intended docking study, in which the most potent carbamide derivatives **12d**, **12e**, **12k**, **12l**, **12p**, **12q**, **12t** and **12u** were docked into the active site of VEGFR-2 kinase (**Figure 3a**).

<Insert Figure 3 here>

Molecular insights of the lead carbamide derivatives **12k** and **12e** (**Figure 3b** & **c**) indicated that both the amino hydrogen atoms of urea linker were able to forms H-bond with the carbonyl oxygen atom of Glu885 (**12e**: N2-H···O: 1.67 Å, N1-H···O: 2.31 Å; **12k**: N2-H···O: 1.66 Å, N1-H···O: 2.33 Å). Whereas the other H-bond was recognised between carbonyl oxygen atom of urea and the amino hydrogen atom of Asp1046 (**12e**: O···H-N: 2.30 Å; **12k**: O···H-N: 2.34 Å) in an extended channel situated straight next to the ATP binding site. On the other hand, the binding pattern of urea functionality for the most active compounds accomplishes a similar binding pattern (hydrogen bonds with Glu885 and Asp1046) as that of co-crystal (sorafenib) by augmenting the hypothesis, with an exception that compound **12t** interacts with Glu815. Consequently, the cyclic secondary amine motifs of **12e** and **12k** (piperidine and pyrrolidine) along with phenyl group of urea moiety achieves a hydrophobic interaction with hydrophobic side chains of Phe1047, Cys1045, Ile1044, Leu1019, Cys1024, Ile1025, Val 899, Ile 888, Leu 889 and Val 914 amino acids of hydrophobic pocket. Apart from this, the thioindole group of other compounds **12p**, **12d** and **12t** shared hydrophobic cleft of Cys1024, Ile1025, Leu1019, Cys1024, Ile892, Ile888 and Leu889, justifying their biological activity. Furthermore, the amino cation of Lys868 forms a pi-cation interaction with the phenyl ring of compounds **12e** and **12k**. From the docking study, it was observed that the most potent compounds in study were well accommodated inside the binding site of the VEGFR-2. To make deeper understanding of our outcomes, we tried the superimposition of the potent ligands **12e** and **12k (Figure 4a)** and the resultant pose reveals that all the structural motifs were superimposed identically with one another suggesting the probable binding mode. The subsequent superimposition poses of sorafenib with the potent ligand **12k** recommend that urea functionality of ligand **12k** occupied identical position with the urea functionality of the sorafenib as noticed in **Figure 4b**. The H-bonding interactions for docking poses along with docking scores were presented in **Table 3** and 2D diagrams were included in the supplementary data.

<Insert Figure 4 here>

<Insert Table 3 here>

3.2 *In silico* ADME/T studies

A set of pharmacokinetic properties for 8 potent molecules were calculated through QikProp program (Qikprop, version 6.5, Schrödinger, LLC, New York, NY, 2014) to examine

drug-likeliness in terms of ADME/T properties [35]. The computed ADME/T parameters of investigated compounds are within their prescribed range as mentioned in **Table 4**. This *in silico* study revealed that all the calculated compounds exhibited adequate values of molecular weight (mol. Wt.), hydrogen bond donors (donor HB), hydrogen bond acceptors (acceptor HB), partition coefficient (QPlogPo/w), and ensuing Lipinski's rule of 5. Comparison of the ADME/T properties of the potent molecules with that of known drug depicts that these conjugates show no violation in the recommended ranges of physico-chemical descriptors, stating that the compounds are not toxic and obeys Lipinski's rule of 5.

<Insert Table 4 here>

3.3 3D-QSAR study

In order to further explore the SARs of pyrimidine-thioindole conjugates, the *in vitro* VEGFR-2 inhibition data was selected to concept the 3D-quantitative structure activity relationship (3D-QSAR) models. Based on the comprehensive procedure manual described in the literature,[36] the IC_{50} values of all derivatives against VEGFR-2 were picked and transformed to pIC_{50} values.

<Insert Table 5 here>

3.3.1 Field and Atom-based 3D-QSAR analysis

The accurate PLS statistics outcomes of the Field and Atom based 3D-QSAR models were disclosed in **Table 5**. The experimental and the predicted pIC_{50} values of the target compounds against VEGFR-2 are listed in **Table 6**. The PLS study elucidates the predictive aptitude and the self-consistence of the model in which, the cross-validation correlation coefficient (q^2) and correlation coefficient (r^2) are two essential measures to figure out the strength of PLS analysis. The cross-validation correlation coefficient of more than 0.3 will be advised statistically as the chance of noticeable correlation being <95%. The q^2 and r^2 of the field based model were 0.689 and 0.43, respectively, and the atom based 3D-QSAR model q^2 and r^2 were 0.481 and 0.43 respectively as tabulated in **Table 5**. The ideal sum of components used to produce field and atom based models were in the acceptable range. The Fisher test results of models were found to be 66.6 and 71.2 respectively. Furthermore, the predicted standard errors of the field and atom-based models were found to be 0.163 and 0.179 respectively. The input of the steric, electrostatic, hydrophobic, hydrogen bond donor and acceptor fields of the field-based model were 37.3%, 11.6%, 24.0%, 16.5% and 10.4%, respectively and the input of the electrostatic, hydrophobic, hydrogen bond donor fields of the atom-based model were 0.7%, 68.9% and 5.0%,

respectively. The obtained results suggested that the field and atom-based models constructed were consistent and supportable modification of the target molecules to pick-up the better activity. The detailed PLS data were shown in **Table 6**.

<Insert Table 6 here>

The linear relationship results in **Figure 5** shown that the calculated pIC_{50} and the experimental pIC_{50} values of the field and atom-based models had a worthy linear relationship. Besides, due to structural variations, a small amplitude instabilities were detected among the calculated pIC_{50} and the experimental pIC_{50} values.

<Insert Figure 5 here>

3.3.2 Countour analysis

In order to understand the impact of various fields on the target property, by Schrodinger software, Field and Atom contour maps were produced to recognise the impression of different fields (the steric field, electrostatic field, hydrophobic field and hydrogen bond donor and acceptor fields) on the activity data of compounds. StDev*Coeff mapping route was used to transform Field and atom-based models into visual results. All contour maps represented 80% level contributions for favored and 20% level contributions for disfavored. As indicated in **Figure 6** and **Figure 7**, the template compound **12e** (with the highest pIC_{50} value) and the compound **12p** were chose to disclose the 3D-QSAR information of field and atom-based models. These results can support to understand the connection between structure and biological activity.

<Insert Figure 6 here>

3.3.2.1 Field-based contour analysis:

According to the field contour maps shown in **Figure 6**, it can be obviously realized that the thioindole ring, benzene ring of urea was covered with a green contour. Thus, it is sensible to introduce the thioindole structure on the pyrimidine ring promoting the VEGFR-2 inhibition. Also, the occupancy of green contours around the 2° amine rings showed the importance of the ring expansion strategy in the designing of titled molecules. Similarly, the results of red contours around the N-atom of 2° amine revealed that antiproliferative activity of the target compound decreased as the volume of the 2° amine ring increased (**12d**, **12l** > **12p**, **12s**). In addition, the presence of a minor amount of yellow contours around the 2° amine ring directed that the hydrophobicity of the 2° amine ring was favorable to uphold the proliferative activity of the

compounds against VEGFR-2 protein. A big cyan contour appeared around the N-H atoms and gray contour around the O-atom of urea functionality indicated that the urea functionality plays an important role in preserving the VEGFR-2 activity of the target compounds.

3.3.2.2 Atom-based contour analysis

<Insert Figure 7 here>

Figure 7 showed the hydrophobic and electron withdrawing cubes of the atom-based model. A group of light-green cubes overlapped around the benzene ring of the urea functionality. It revealed that the electron withdrawing substitutions on the benzene ring is beneficial to increase the VEGFR-2 inhibition (R = 4-Cl > 2-CH_3-4-Cl > H > 4-OMe > 3,5-diOMe). In the atom-based model, we observed that the orange-yellow cubes appeared around the pyrimidine ring, indicating that this region would be conducive to maintain the proliferative activity of the compounds against VEGFR-2 protein.

4.0 Structure Activity Relationships (SARs)

Structure activity relationship (SAR) of the synthesized compounds was shaped (**Figure 8**) to study the impact of substitution on pyrimidine ring in comparison with the inhibitory activity against human cancer cell lines as well as VEGFR-2.

Comparing the activity of compounds **12a–aa** in relation to cytotoxicity revealed that the presence of non-aromatic nitrogen heterocycles (**12b-i**, **12k**, **12l**) and strained cyclopropyl ring (**12u** & **12v**) at C6-position of pyrimidine were active particularly towards breast cancer cell lines (MDA-MB-231). Primary aromatic amines (**12m**, **12w-aa**) have deviated the cytotoxicity profile against all the tested cancer cell lines, except that, the compounds **12y**, **12z** & **12aa** bearing 3,5-dimethoxy and 4-chloro-phenyl exhibited good activity against PC-3 and MDA-MB-231 cell lines respectively. In specific, the presence of five-membered pyrrolidine ring (**12k**) favoured the good anticancer effects against all the selected cancer cell lines. Both *N*-substituted (**12n**, **12p**, **12q**) as well as saturated nitrogen heterocycles (**12a**, **12d**, **12e**, **12k** and **12l**) were found to be endurable towards liver cancer cell lines (HepG2).

Relating the inhibitory concentration of compounds **12b–i** and **12k**, **12l**, **12q**, **12t**, **12v**, **12z**, **12aa** indicated that both the introduction of electron donating (4-methoxy, 2,5-dimethyl, 2,5-

dimethoxy) as well as electron withdrawing (4-chloro, 2-methyl-4-chloro) groups were found to be tolerable on aryl urea.

<Insert Figure 8 here>

Conversely, in relation to VEGFR-2 inhibition, the introduction of non-aromatic nitrogen heterocycles such as morpholine, pyrrolidine, piperidine **12a**–**l** and *N*-substituted piperazines **12n**–**t** (*N*-benzyl, *N*-pyridyl) at C6-position of pyrimidine resulted in significant to moderate VEGFR-2 inhibition (IC_{50} ranging from 0.31 to 4.86 μM). Compounds with primary aromatic amines (**12m** and **12w**–**aa**) exhibited the moderate inhibitory action on VEGFR-2 (IC_{50} ranging from 1.33 to 3.51 μM). Similarly, introduction of strained functionality like cyclopropyl amine **12u** also afforded the most active VEGFR-2 inhibition (IC_{50} 0.44 μM).

Finally, we focused the effect of substitution on phenyl urea at C2-position of pyrimidine. Introduction of chloro group at *para* position of phenyl urea **12k** (IC_{50} 0.33 μM) resulted in about 8 and 10-fold rise in enzyme inhibition relative to the electron donating **12j** and unsubstituted analogue **12i** (IC_{50} 2.61 μM and 3.23 μM) respectively. Also, with compounds **12c** and **12f** bearing chloro group was shown substantial inhibition (IC_{50} 1.44 μM, 1.82 μM respectively). On the other hand, 2-methyl-4-chloro substitution (**12d**, **12l** and **12p**) displayed similar levels of enzyme inhibition (IC_{50} ranging from 0.35 to 0.92 μM) with all the non-aromatic nitrogen heterocycles, highlighting the impact of this group for VEGFR-2 inhibition. The same trend was observed with comparison of 2-methyl-4-chloro and unsubstituted phenyl urea with cyclopropyl (IC_{50} 0.44 μM > 5.22 μM; **12u** was 12-fold > **12v**) and phenylamino rings (IC_{50} 1.33 μM > 2.74 μM; **12w** > **12m**) respectively. Similarly, incorporation of 2-methyl-4-chloro along with bulky benzyl piperazine **12s** (IC_{50} 4.86 μM) led to non-significant activity. The unsubstituted phenyl group **12a**, **12h**, **12n** and **12q** also led to significant to reasonable VEGFR-2 suppressive activity (IC_{50} ranging from 0.67 to 4.55 μM). Concerning the influence of electron donating substitutions like 2,5 dimethyl **12e**, **12r**, **12x**, **12t** (IC_{50} ranging from 0.31 to 2.82 μM) > 4-methoxy **12b**, **12g**, **12j**, **12o**, **12z** (IC_{50} ranging from 1.13 to 4.15 μM) > 2,5 dimethoxy **12y** (IC_{50} 3.51 μM) exhibited potent to moderate VEGFR-2 suppressive activity. Grafting of mercapto indole at C4-position of pyrimidine was well tolerated for both *in vitro* anticancer effects on human cell lines and VEGFR-2 inhibition.

5.0 HUVECs tube formation assay

Tube formation assay is the most widely used *in vitro* assay in which capacity of endothelial cells, overlaid at sub-confluent densities will be measured to model the reorganization stage of angiogenesis. Typically, this assay is employed to measure the ability of the anti-angiogenic compounds to promote or inhibit capillary-like structures (tubes) which could be useful to study the underlying mechanisms in cancer [37]. To study the anti-angiogenic properties of the potent compound **12k**, matrigel tube formation assay of HUVECs was performed. As shown in **Figure 9**, treatment given with compound **12k** at 2.5 and 5 µM was significantly inhibited the networks of HUVECs in wells where elongated, robust networks clearly seen in wells seeded with untreated. The results of the matrigel assay demonstrated that compound **12k** inhibited the formation of HUVEC tube like structures in a dose dependant manner where similar effects were noticed with standard drug sorafenib. In addition, quantification of tube formation assay was analysed using WimTube analysis [38] which are highlighting the remarkable antiangiogenic properties of the compound **12k** with sorafenib (**Figure S2**) where all aspects of network formation were significantly affected in compound treated wells, as indicated by a decrease of cell-covered area, tube length, branching points and total loops (**Figure S3**).

<Insert Figure 9 here>

5.1 Cell invasion/transwell assay

Cell migration and invasion are the two main essential steps for the formation of new blood vessels during the angiogenesis processes which lead to angiogenesis and metastasis [39]. Herein, we proceeded with Boyden chamber (Transwell) assay in HUVECs to determine the ability of cancer cells to pass through the Matrigel and membrane barriers with 2.5 and 5 µM of compound **12k** where sorafenib used as a standard and results were shown in **Figure 10**. In control, majority of the cells migrated to the bottom layer of the Boyden chamber where invaded cells were significantly reduced by **12k**. In the results, it was clearly indicating that compound **12k** preventing the cell invasion in a dose dependant manner.

<Insert Figure 10 here>

5.2 Colony forming assay

The proliferative potential and ability of adherent cells to form distinct colonies from a single cell can be assessed using the colony formation assay. Hence, it is the method of choice to define the effectiveness of cytotoxic agents based on cell survival and cell reproductive death [40]. In this assay, the colony forming ability of MDA-MB-231 cells was measured by treating with media containing different concentrations (1, 3 and 5 µM) of compound **12k** over a period of 7 days to form colonies. The cells were then stained with crystal violet to visualise colonies and from **Figure 11**, it clearly directs the potential of **12k** in inhibition of colony formation as compared to the control and so it could be one of the mechanisms reflected in prompting cytotoxic activity in MDA-MB-231 cancer cells.

<Insert Figure 11 here>

5.3 Wound healing assay (migration assay)

Cell migration is a vital possession involved in the dissemination of cancerous cells mostly during cancer metastasis. The cell culture wound-closure is of particular interest to examine the inhibition of migration for effective cancer treatment [41]. A wound healing assay was performed on MDA-MB-231 cells to study the inhibitory influence of compound **12k** and sorafenib on migration ability. In this protocol, wounds were made on highly metastases confluent cell monolayers of MDA-MB-231 by scratching with a sterile pipette tip and picturing the response using phase contrast microscopy. As shown in **Figure 12**, after 24 h, the cells treated with 2.5 µM of compound **12k** and sorafenib displayed considerable inhibition of cell migration compared to the control cells, while migration was totally significant after treatment with a 5 µM solutions.

<Insert Figure 12 here>

6.0 Apoptosis detection studies

6.1 Identification of apoptotic cells

Conception of cell death, principally apoptosis is one of the most-widely studied scenarios in cancer. Effect of chemotherapeutic agents on morphological hallmarks of apoptosis like chromatin condensation, nuclear fragmentation and pyknosis is of high value to examine using fluorescent staining techniques. Hoechst is a cell-permeate nuclear counter stain, binds

immutably to the DNA minor groove at A–T-rich clusters with specific staining of living or fixed nuclei. Binding of Hoechst to ds DNA emits blue fluorescence, stains the condensed chromatin in apoptotic cells further deeply than the chromatin in normal cells [42]. Hence, apoptotic cells come out brighter reasonably than live cells. As exposed in **Figure 13**, the control (a), cell nuclei preserve intact showing usual morphology whereas, the MDA-MB-231 cells treated with 2.5 µM (b & d) and 5 µM (c & e) of compounds **12e** and **12k** respectively exhibited the typical apoptotic features together with nuclear shrinkage, pyknotic or fragmented bright nuclei, and chromatin condensation in a dose-dependent manner.

<Insert Figure 13 here>

6.2 Quantification of apoptosis induction

Annexin V-FITC/Propidium iodide dual staining assay assists the discrepancy between necrotic cells (Q1-UL; AV-/PI+), late apoptotic cells (Q1- UR; AV+/PI+), early apoptotic cells (Q3-LR; AV+/PI-) and live cells (Q2-LL; AV-/PI-) using flow cytometry. In view of high affinity towards phosphatidylserine (PS), Annexin V (Annexin V-FITC) identifies the apoptotic cells, in which exteriorization of PS occurs as a normal process of apoptosis [43]. MDA-MB-231 breast cancer cells were treated with compound **12k** at different concentrations of 2.5 and 5 µM. It can be observed from **Figure 14** that the percentage of late and early apoptotic cells significantly improved from 3.8 to 11.2% and 19.4 to 36.6% respectively with increase in the concentration from 2.5 to 5 µM concentration, which signifies the dose-dependent apoptosis induction on MDA-MB-231 breast cancer cells.

<Insert Figure 14 here>

6.3 Effect on mitochondrial membrane potential (DΨm)

Distinct aspects of mitochondria function is a key indicator of cell health, chiefly associates with the generation of mitochondrial membrane potential (MMP) *via* ATP synthesis through a series of redox reactions. Variations in the redox equilibration of the mitochondrial membrane presumed to enhance the generation of reactive oxygen species (ROS) and thereby loss of mitochondrial membrane potential (DΨm) [44]. Hence, it is an influential undertaking to consider the effect of compound **12k** on mitochondrial membrane potential (DΨm). The membrane-permeate JC-1 dye was used for defining DΨm, in which J-monomers in depolarized

mitochondria, therefore, stains green in color whereas healthy mitochondria consist of J-aggregates, thus stains red in color. MDA-MB-231 cells were treated with 2.5 µM (b & d) and 5 µM (c &e) of compounds **12e** and **12k** respectively where proportionality was observed in depolarized cell population with rise in the concentration. Loss of membrane integrity was observed in a dose-dependent manner as shown in **Figure 15**.

<Insert Figure 15 here>

6.4 Effect on intracellular ROS generation

Cells are supplied with a controlling antioxidant defense structure to battle extreme production of ROS enhanced free radical generation, crushes the cells' natural antioxidant defenses, leads to the destruction of mitochondrial potential thereby causes apoptosis [45]. Therefore, to observe the degree of ROS generation by compound **12k**, the intracellular ROS generation was driven using the Carboxy-H_2DCFDA staining. MDA-MB-231 cells were treated with different doses of compound **12e** and **12k**, in which DCFDA is reacted to form 2',7'-dichlorofluorescein (DCF) in the existence of ROS generation, led to increase in green fluorescence with increase in the concentration. From **Figure 16**, it certainly indicates dose dependency in inducing ROS generation as compared to the control and thus it might be one of the reflected mechanisms in instigation of apoptosis in MDA-MB-231 breast cancer cells.

<Insert Figure 16 here>

7.0 Conclusion

In summary, the present study organically highlights the design, synthesis and biological evaluation of carbamide derived pyrimidine-thioindole conjugates, in which a series of 27 molecules were synthesized by using molecular hybridization approach from the known VEGFR-2 inhibitors. Justification of anticancer effects by means of *in vitro* VEGFR-2 inhibition sets the origin towards the identification of possible mechanism for cytotoxicity at molecular level. From the initial screening, it was inferred that among the synthesized compounds, 8 compounds i.e. **12d**, **12e**, **12k**, **12l**, **12p**, **12q**, **12t** and **12u** prominently suppressed VEGFR-2, with IC_{50} values of 310 to 920 nM in contrast to the positive control, sorafenib 210 nM. The enzymatic inhibition results also evidenced that all the synthesized compounds were found to unveil substantial cytotoxicity against VEGFR-2 protein with IC_{50} 0.31 ± 0.07 to 5.22 ± 0.42

µM. Later, *in vitro* antiproliferative effects of these derivatives were also evaluated against a certain human cancer cell lines. The Structure Activity Relationship (SAR) studies pointed that, substitution of cyclic secondary amines with 3-methyl-4-chloro group on aryl urea seems to be the central aspect for affecting the VEGFR-2 activity of the proposed structural motifs. The mechanism of cellular toxicity in MDAMB-231 was established through apoptosis induction by depolarization of mitochondrial membrane potential, increased ROS production and subsequent DNA damage. In addition, clonogenic and wound healing assays indicated the inhibition of colony formation and cell migration by **12k** in a dose-dependent manner. Angiogenesis inhibition was evident by HUVECs tube formation assay and cell invasion by transwell assay. Molecular modeling studies supported the possible binding mode of 8 potent molecules to the catalytic cleft of VEGFR-2 protein. All the potent molecules exhibited pleasing ADMET property results (obeys the Lipinski rule of 5). Inclusively, the newly synthesized pyrimidylphenylurea derivatives can be developed as prospective anticancer agents through VEGFR-2 inhibition and apt structural reforms may succeed in breeding promising anticancer agents.

8.0 Experimental section

8.1 Chemistry

General Methods. All the reagents and solvents were obtained from commercial suppliers and were used without further purification. Analytical thin layer chromatography (TLC) was performed on MERCK pre-coated silica gel 60-F254 (0.5 mm) aluminum plates. Visualization of the spots on TLC plates was achieved by UV light. ^{1}H and ^{13}C NMR spectra were recorded on Bruker 500 MHz by making a solution of samples in the DMSO-d_6 as solvent using tetramethyl silane (TMS) as the internal standard. Chemical shifts for ^{1}H and ^{13}C are reported in parts per million (ppm) downfield from tetra methyl silane. Spin multiplicities are described as s (singlet), brs (broad singlet), d (doublet), t (triplet), q (quartet), and m (multiplet). Coupling constant (*J*) values are reported in *hertz* (Hz). HRMS were determined with Agilent QTOF mass spectrometer 6540 series instrument. Wherever required, column chromatography was performed using silica gel (60-120; 100-200). The reactions wherever anhydrous conditions required are carried under nitrogen positive pressure using freshly distilled solvents. All evaporation of solvents was carried out under reduced pressure using rotary evaporator below 45

^{o}C. Melting points were determined with an electro thermal digital melting point apparatus IA9100 and are uncorrected. The names of all the compounds given in the experimental section were taken from ChemBioDraw Ultra, Version 12.0.

*8.1.1 6-((1H-Indol-3-yl)thio)-N^4-substituted amino pyrimidine-2,4-diamine (**10a-i**)*

To a mixture of amino derivatives of pyrimidine (**9a–i**, 1 equiv.), indole-3-thiol (**3**, 2.5 equiv.), potassium iodide (1.5 equiv.) in ethanol, under 80 ^{o}C was added triethyl amine and stirred under reflux till complete consumption of the starting materials as determined by TLC. The solvent was then removed using rotary evaporator and extracted using ethyl acetate (25 mL x 3) and water. The organic layer was concentrated under *in vacuo* and the residue obtained was chromatographed on silica gel (elution with hexane/EtOAc = 7:3-5:5) to provide the 6-((1*H*-indol-3-yl)thio)-*N*^{4}-substituted amino pyrimidine-2,4-diamine derivatives **10a-i** in good yields.

*8.1.2 1-(4-((1H-Indol-3-yl)thio)-6-aminopyrimidin-2-yl)-3-arylurea (**12a-aa**)*

To a mixture of 4-((1*H*-indol-3-yl)thio)-6-aminopyrimidin-2-amine (**10a-i**, 1 equiv.) in dioxane, substituted aryl isocyanates (**11a-f**, 1 equiv.) were added under 100 ^{o}C and stirred till complete consumption of the starting materials as determined by TLC. The reaction mixture was then quenched with water and extracted using ethyl acetate (25 mL x 3). The organic layer was concentrated under *in vacuo* and the residue obtained was chromatographed on silica gel (elution with hexane/EtOAc = 8:2-4:6) to provide the 1-(4-((1*H*-indol-3-yl)thio)-6-aminopyrimidin-2-yl)-3-arylurea **12a-aa** in moderate to good yields.

*8.1.2.1 1-(4-((1H-Indol-3-yl)thio)-6-morpholinopyrimidin-2-yl)-3-phenylurea (**12a**)*

White solid; yield 83%; mp: 185-189 ^{o}C; FT-IR (cm^{-1}): 3365, 3116, 2922, 2862, 1897, 1710, 1370, 738; ^{1}H NMR (500 MHz, DMSO-d_6): δ 11.80 (s, 1H), 11.16 (s, 1H), 9.50 (s, 1H), 7.84 (s, 1H), 7.49–7.44 (m, 2H), 7.24 (dd, J = 23.6, 16.0 Hz, 3H), 7.18 (d, J = 7.9 Hz, 1H), 7.10 (dd, J = 13.4, 7.7 Hz, 3H), 5.92 (s, 1H), 3.57 (s, 8H); ^{13}C NMR (125 MHz, DMSO-d_6): δ 165.2, 156.3, 152.4, 146.1, 144.5, 134.5, 129.7, 129.2, 128.9, 128.0, 128.0, 127.2, 126.9, 126.8, 124.3, 119.2, 107.5, 102.0, 64.3, 60.3, 54.5, 14.3; HRMS (ESI): *m/z* calculated for $C_{23}H_{23}N_6O_2S$ 447.1603 found 447.1628 $[M+H]^+$.

*8.1.2.2 1-(4-((1H-Indol-3-yl)thio)-6-morpholinopyrimidin-2-yl)-3-(3-methoxyphenyl)urea (**12b**)*

White solid; yield 86%; mp: 183-186 ^{o}C; FT-IR (cm^{-1}): 3373, 3116, 2922, 2876, 1834, 1715, 1693, 1487, 754; ^{1}H NMR (500 MHz, DMSO-d_6): δ 11.78 (s, 1H), 10.93 (s, 1H), 9.42 (s, 1H), 7.83 (s, 1H), 7.47 (dd, J = 13.6, 5.4 Hz, 2H), 7.20 (d, J = 7.3 Hz, 1H), 7.11 (t, J = 7.2 Hz, 1H), 6.94 (d, J = 8.7 Hz, 2H), 6.83 (d, J = 8.7 Hz, 2H), 5.97 (s, 1H), 3.73 (s, 3H), 3.59 (s, 4H), 3.48 (s, 2H), 3.16 (s, 2H); ^{13}C NMR (125 MHz, DMSO-d_6): δ 169.8, 161.8, 157.1, 155.5, 152.1, 137.1, 133.1, 131.7, 122.8, 121.3, 120.8, 118.7, 114.3, 113.0, 96.5, 91.7, 66.0, 55.6, 44.2; HRMS (ESI): *m/z* calculated for $C_{24}H_{25}N_6O_3S$ 477.1709 found 477.1724 $[M+H]^+$.

*8.1.2.3 1-(4-((1H-Indol-3-yl)thio)-6-morpholinopyrimidin-2-yl)-3-(3-chlorophenyl)urea (**12c**)*

Yellow solid; yield 85%; mp:178-182 ^{o}C; FT-IR (cm^{-1}): 3368, 3119, 2927, 2868, 1839, 1788, 1367, 758; ^{1}H NMR (500 MHz, DMSO-d_6): δ 11.80 (s, 1H), 11.19 (s, 1H), 9.59 (s, 1H), 7.84 (s, 1H), 7.47 (d, J = 8.1 Hz, 1H), 7.43 (d, J = 7.9 Hz, 1H), 7.29 (d, J = 8.8 Hz, 2H), 7.18 (t, J = 7.1 Hz, 1H), 7.10 (t, J = 7.6 Hz, 1H), 6.99 (d, J = 8.8 Hz, 2H), 6.03 (s, 1H), 3.60 (s, 4H), 3.41 (s, 4H); ^{13}C NMR (125 MHz, DMSO-d_6): δ 169.4, 161.8, 157.0, 152.0, 137.7, 137.1, 133.0, 129.4, 128.9, 126.8, 122.8, 121.1, 120.8, 118.7, 113.0, 96.5, 92.0, 66.0, 44.2; HRMS (ESI): *m/z* calculated for $C_{23}H_{22}ClN_6O_2S$ 481.1213 found 481.1240 $[M+H]^+$.

*8.1.2.4 1-(4-((1H-Indol-3-yl)thio)-6-morpholinopyrimidin-2-yl)-3-(4-chloro-2-methylphenyl)urea (**12d**)*

White solid; yield 76%; mp:183-185 ^{o}C; FT-IR (cm^{-1}): 3372, 3112, 2927, 2856, 1839, 1788, 1367, 748; ^{1}H NMR (500 MHz, DMSO-d_6): δ 11.79 (s, 1H), 11.22 (s, 1H), 9.61 (s, 1H), 7.84 (d, J = 2.6 Hz, 1H), 7.57 (d, J = 1.9 Hz, 1H), 7.48 (d, J = 8.1 Hz, 1H), 7.44 (d, J = 7.8 Hz, 1H), 7.20 (dd, J = 14.1, 7.7 Hz, 2H), 7.11 (t, J = 7.4 Hz, 1H), 6.56 (dd, J = 8.2, 1.8 Hz, 1H), 5.93 (s, 1H), 3.62–3.55 (m, 4H), 3.38 (s, 4H), 2.27 (s, 3H); ^{13}C NMR (125 MHz, DMSO-d_6): δ 169.8, 161.5, 158.9, 157.0, 152.0, 148.0, 137.9, 133.5, 133.1, 131.5, 128.8, 122.8, 119.7, 118.3, 113.6, 113.0, 96.5, 91.8, 44.1, 43.5, 19.3; HRMS (ESI): *m/z* calculated for $C_{24}H_{24}ClN_6O_2S$ 495.1370 found 495.1397 $[M+H]^+$.

*8.1.2.5 1-(4-((1H-Indol-3-yl)thio)-6-(piperidin-1-yl)pyrimidin-2-yl)-3-(2,5-dimethylphenyl)urea (**12e**)*

White solid; yield 86%; mp:179-184 ^{o}C; FT-IR (cm^{-1}): 3376, 3115, 2949, 2832, 1837, 1768, 1347, 774; ^{1}H NMR (500 MHz, DMSO-d_6): δ 11.44 (s, 1H), 10.04 (s, 1H), 9.15 (s, 1H), 7.68 (s,

1H), 7.37 (s, 1H), 7.05 (s, 3H), 6.96 (d, *J* = 7.0 Hz, 3H), 6.06 (s, 1H), 3.43 (s, 4H), 1.89 (s, 6H), 1.58 (s, 2H), 1.43 (s, 4H); ^{13}C NMR (125 MHz, DMSO-d_6): δ 169.1, 161.3, 157.4, 152.7, 136.8, 135.6, 134.9, 132.8, 128.7, 127.8, 126.4, 122.4, 120.5, 118.2, 112.5, 96.5, 91.3, 45.0, 25.5, 24.4, 18.5, 18.3; HRMS (ESI): *m/z* calculated for $C_{26}H_{29}N_6OS$ 473.2124 found 473.2163 $[M+H]^+$.

*8.1.2.6 1-(4-((1H-Indol-3-yl)thio)-6-(piperidin-1-yl)pyrimidin-2-yl)-3-(4-chlorophenyl)urea (**12f**)*

White solid; yield 89%; mp:189-192 ^oC; FT-IR (cm^{-1}): 3372, 3118, 2949, 2822, 1827, 1799, 1370, 747; ^{1}H NMR (500 MHz, DMSO-d_6): δ 11.79 (s, 1H), 11.32 (s, 1H), 9.53 (s, 1H), 7.84 (d, *J* = 2.5 Hz, 1H), 7.48 (d, *J* = 8.1 Hz, 1H), 7.44 (d, *J* = 7.9 Hz, 1H), 7.30 (d, *J* = 8.7 Hz, 2H), 7.19 (t, *J* = 7.5 Hz, 1H), 7.11 (t, *J* = 7.4 Hz, 1H), 7.05 (d, *J* = 8.7 Hz, 2H), 5.93 (s, 1H), 3.37 (d, *J* = 26.1 Hz, 4H), 1.56 (d, *J* = 4.2 Hz, 2H), 1.43 (s, 4H); ^{13}C NMR (125 MHz, DMSO-d_6): δ 169.3, 161.7, 159.0, 157.4, 148.0, 138.0, 136.8, 135.6, 135.0, 128.7, 127.8, 126.3, 122.4, 120.5, 118.2, 113.6, 107.6, 96.3, 44.4, 18.6, 18.4; HRMS (ESI): *m/z* calculated for $C_{24}H_{24}ClN_6OS$ 479.1421 found 479.1452 $[M+H]^+$.

*8.1.2.7 1-(4-((1H-Indol-3-yl)thio)-6-(piperidin-1-yl)pyrimidin-2-yl)-3-(4-methoxyphenyl)urea (**12g**)*

White solid; yield 87%; mp:187-190 ^oC; FT-IR (cm^{-1}): 3366, 3111, 2922, 2853, 1822, 1733, 1398, 762; ^{1}H NMR (500 MHz, DMSO-d_6): δ 11.77 (s, 1H), 11.06 (s, 1H), 9.34 (s, 1H), 7.82 (s, 1H), 7.45–7.33 (m, 2H), 7.22–7.16 (m, 1H), 7.11 (t, *J* = 7.5 Hz, 1H), 7.01 (d, *J* = 9.0 Hz, 2H), 6.85 (d, *J* = 15.4 Hz, 2H), 5.85 (s, 1H), 3.76–3.72 (m, 3H), 3.37 (s, 4H), 1.56 (s, 2H), 1.43 (s, 4H);^{13}C NMR (125 MHz, DMSO-d_6): δ 169.7, 161.1, 157.2, 155.5, 152.1, 137.1, 133.1, 131.8, 128.8, 122.7, 121.2, 120.7, 120.4, 118.7, 114.4, 113.0, 96.8, 91.4, 55.6, 45.1, 25.3, 24.3; HRMS (ESI): *m/z* calculated for $C_{25}H_{27}N_6O_2S$ 475.1916 found 475.1949 $[M+H]^+$.

*8.1.2.8 1-(4-((1H-Indol-3-yl)thio)-6-(piperidin-1-yl)pyrimidin-2-yl)-3-phenylurea (**12h**)*

Yellow solid; yield 85%; mp:190-196 ^oC; FT-IR (cm^{-1}): 3369, 3119, 2982, 2843, 1838, 1892, 1489, 742; ^{1}H NMR (500 MHz, DMSO-d_6): δ 11.81 (s, 1H), 11.29 (s, 1H), 9.46 (s, 1H), 7.84 (s, 1H), 7.49 (d, *J* = 8.1 Hz, 1H), 7.45 (d, *J* = 7.9 Hz, 1H), 7.27 (t, *J* = 7.9 Hz, 2H), 7.20 (t, *J* = 7.2 Hz, 1H), 7.15 (d, *J* = 7.8 Hz, 2H), 7.11 (t, *J* = 7.4 Hz, 1H), 7.01 (t, *J* = 7.3 Hz, 1H), 5.82 (s, 1H), 3.37 (s, 4H), 1.56 (s, 2H), 1.42 (s, 4H); ^{13}C NMR (125 MHz, DMSO-d_6): δ 169.7, 161.1, 157.2, 155.5, 152.1, 137.1, 133.1, 131.8, 128.8, 122.7, 121.2, 120.7, 120.4, 118.7, 114.4, 113.0,

96.8, 91.4, 55.6, 45.1, 25.3, 24.3; HRMS (ESI): *m/z* calculated for $C_{24}H_{25}N_6OS$ 445.1811 found 445.1835 $[M+H]^+$.

*8.1.2.9 1-(4-((1H-Indol-3-yl)thio)-6-(pyrrolidin-1-yl)pyrimidin-2-yl)-3-phenylurea (**12i**)*

White solid; yield 83%; mp:198-202 ^oC; FT-IR (cm^{-1}): 3372, 3118, 2922, 2853, 1832, 1793, 1389, 752; ^1H NMR (500 MHz, DMSO-d_6): δ 11.79 (s, 1H), 11.53 (s, 1H), 9.49 (s, 1H), 7.85 (s, 1H), 7.51 (d, J = 8.1 Hz, 1H), 7.46 (d, J = 7.9 Hz, 1H), 7.38 (d, J = 7.9 Hz, 2H), 7.30 (t, J = 7.8 Hz, 2H), 7.22 (t, J = 7.5 Hz, 1H), 7.12 (t, J = 7.4 Hz, 1H), 7.03 (t, J = 7.3 Hz, 1H), 5.37 (s, 1H), 3.51 (s, 2H), 2.80 (s, 2H), 1.83 (s, 4H); ^{13}C NMR (125 MHz, DMSO-d_6): δ 170.2, 159.1, 156.8, 152.2, 139.0, 137.1, 133.1, 129.3, 128.7, 123.2, 122.8, 120.7, 119.5, 118.7, 112.9, 96.9, 91.7, 46.6, 24.8; HRMS (ESI): $C_{23}H_{23}N_6OS$ 431.1654 found 431.1683 $[M+H]^+$.

*8.1.2.10 1-(4-((1H-Indol-3-yl)thio)-6-(pyrrolidin-1-yl)pyrimidin-2-yl)-3-(4-methoxyphenyl)urea (**12j**)*

White solid; yield 90%; mp:172-176 ^oC; FT-IR (cm^{-1}): 3370, 3116, 2983, 2868, 1849, 1765, 1368, 748; ^1H NMR (500 MHz, DMSO-d_6): δ 11.79 (s, 1H), 11.35 (s, 1H), 9.41 (s, 1H), 7.82 (s, 1H), 7.51 (d, J = 8.0 Hz, 1H), 7.45 (d, J = 7.8 Hz, 1H), 7.26 (d, J = 8.6 Hz, 2H), 7.22 (t, J = 7.5 Hz, 1H), 7.12 (t, J = 7.3 Hz, 1H), 6.88 (d, J = 8.7 Hz, 2H), 5.38 (s, 1H), 3.73 (s, 3H), 3.50 (s, 2H), 2.81 (s, 2H), 1.82 (s, 4H); ^{13}C NMR (125 MHz, DMSO-d_6): δ 170.2, 159.1, 156.9, 155.5, 152.2, 137.1, 133.1, 132.0, 128.7, 122.8, 121.2, 120.7, 118.7, 114.5, 112.9, 96.9, 91.6, 55.6, 46.0, 24.79; HRMS (ESI): *m/z* calculated for $C_{24}H_{25}N_6O_2S$ 461.1760 found 461.1794 $[M+H]^+$.

*8.1.2.11 1-(4-((1H-Indol-3-yl)thio)-6-(pyrrolidin-1-yl)pyrimidin-2-yl)-3-(4-chlorophenyl)urea (**12k**)*

White solid; yield 89%; mp:170-175 ^oC; FT-IR (cm^{-1}): 3378, 3119, 2973, 2853, 1839, 1714, 1398, 748; ^1H NMR (500 MHz, DMSO-d_6): δ 11.79 (s, 1H), 11.53 (s, 1H), 9.49 (s, 1H), 7.85 (s, 1H), 7.51 (d, J = 8.1 Hz, 1H), 7.46 (d, J = 7.9 Hz, 1H), 7.38 (d, J = 7.9 Hz, 2H), 7.30 (t, J = 7.8 Hz, 1H), 7.22 (t, J = 7.5 Hz, 1H), 7.12 (t, J = 7.4 Hz, 1H), 7.03 (t, J = 7.3 Hz, 1H), 5.37 (s, 1H), 3.51 (s, 2H), 2.80 (s, 2H), 1.83 (s, 4H); ^{13}C NMR (125 MHz, DMSO-d_6): δ 168.8, 160.3, 156.3, 154.6, 151.3, 136.3, 132.2, 131.0, 127.9, 121.9, 120.3, 119.9, 119.5, 117.8, 113.5, 112.1, 95.9, 90.5, 44.2, 24.5; HRMS (ESI): *m/z* calculated for $C_{23}H_{22}ClN_6OS$ 465.1264 found 465.1286 $[M+H]^+$.

*8.1.2.12 1-(4-((1H-Iindol-3-yl)thio)-6-(pyrrolidin-1-yl)pyrimidin-2-yl)-3-(4-chloro-2-methyl phenyl)urea (**12l**)*

Off-white solid, yield 85%; mp:185-189 ^{o}C; FT-IR (cm^{-1}): 3348, 3012, 2972, 2853, 1864, 1710, 1388, 753; ^{1}H NMR (500 MHz, DMSO-d_6): δ 11.37 (s, 1H), 9.97 (s, 1H), 9.08 (s, 1H), 7.61 (s, 1H), 7.30 (s, 1H), 6.98 (s, 3H), 6.89 (d, J = 7.0 Hz, 3H), 5.99 (s, 1H), 3.37 (s, 4H), 2.18 (s, 3H), 1.36 (s, 4H); ^{13}C NMR (125 MHz, DMSO-d_6): δ 167.4, 159.6, 155.7, 151.0, 135.1, 133.9, 133.2, 131.1, 127.0, 126.1, 124.7, 120.8, 118.8, 116.5, 110.8, 94.8, 89.7, 43.4, 23.8, 22.7, 16.8; HRMS (ESI): *m/z* calculated for $C_{24}H_{24}ClN_6OS$ 479.1421 found 479.1452 [M+H]$^{+}$.

*8.1.2.13 1-(4-((1H-Indol-3-yl)thio)-6-(phenylamino)pyrimidin-2-yl)-3-phenylurea (**12m**)*

Yellow solid; yield 87%; mp: 193-197 ^{o}C; FT-IR (cm^{-1}): 3358, 3212, 2976, 2876, 1862, 1712, 1609, 1395, 755; ^{1}H NMR (500 MHz, DMSO-d_6): δ 11.91 (s,1H), 11.58 (s, 1H), 9.38 (s, 1H), 8.94 (s, 1H), 8.01 (d, J = 8.4 Hz, 2H), 7.85 (d, J = 7.5 Hz, 1H), 7.77 (d, J = 7.0 Hz, 1H), 7.72 (d, J = 8.1 Hz, 2H), 7.62 (s, 1H), 7.48 (d, J = 8.2 Hz, 1H), 7.44–7.40 (m, 2H), 7.34 (d, J = 7.3 Hz, 2H), 7.27 (d, J = 6.4 Hz, 2H), 6.98 (t, J = 7.7 Hz, 1H), 6.90 (t, J = 7.4 Hz, 1H); ^{13}C NMR (125 MHz, DMSO-d_6): δ 169.8, 161.5, 158.9, 157.0, 152.0, 148.0, 137.9, 137.1, 133.5, 133.1, 131.5, 129.8, 128.8, 122.8, 120.8, 119.7, 118.7, 118.3, 113.6, 113.0, 107.5, 96.5, 91.8; HRMS (ESI): *m/z* calculated for $C_{25}H_{21}N_6OS$ 453.1498 found 453.1506 [M+H]$^{+}$.

*8.1.2.14 1-(4-((1H-Indol-3-yl)thio)-6-(4-(pyridin-2-yl)piperazin-1-yl)pyrimidin-2-yl)-3-phenylurea (**12n**)*

Light brown solid; yield 76%; mp: 195-198 ^{o}C; FT-IR (cm^{-1}): 3368, 3112, 2967, 2886, 1878, 1705, 1619, 1385, 765; ^{1}H NMR (500 MHz, DMSO-d_6): δ 11.82 (s, 1H), 11.21 (s, 1H), 9.53 (s, 1H), 8.11 (s, 1H), 7.85 (s, 1H), 7.54 (t, J = 7.8 Hz, 1H), 7.48 (dd, J = 15.8, 8.1 Hz, 2H), 7.27 (t, J = 7.9 Hz, 2H), 7.21 (t, J = 7.6 Hz, 1H), 7.12 (t, J = 6.9 Hz, 3H), 7.02 (t, J = 7.3 Hz, 1H), 6.82 (d, J = 8.6 Hz, 1H), 6.68–6.63 (m, 1H), 5.96 (s, 1H), 3.54 (s, 8H); ^{13}C NMR (125 MHz, DMSO-d_6): δ 169.9, 161.6, 159.0, 157.1, 152.0, 148.0, 138.8, 138.0, 137.2, 133.2, 129.2, 128.8, 123.2, 122.8, 120.8, 119.6, 118.7, 113.6, 113.0, 107.6, 96.5, 91.7, 44.2, 43.5; HRMS (ESI): *m/z* calculated for $C_{28}H_{27}N_8OS$ 523.2029 found 523.2052 [M+H]$^{+}$.

*8.1.2.15 1-(4-((1H-Indol-3-yl)thio)-6-(4-(pyridin-2-yl)piperazin-1-yl)pyrimidin-2-yl)-3-(4-methoxyphenyl)urea (**12o**)*

White solid; yield 79%; mp: 188-189 ^{o}C; FT-IR (cm^{-1}): 3370, 3113, 2967, 2881, 1896, 1702, 1609, 1395, 755; ^{1}H NMR (500 MHz, DMSO-d_6): δ 11.80 (s, 1H), 11.18 (s, 1H), 9.48 (s, 1H), 7.83 (s, 1H), 7.48–7.43 (m, 2H), 7.32 (dd, J = 14.4, 7.3 Hz, 4H), 7.26–7.22 (m, 2H), 7.18 (t, J = 7.5 Hz, 1H), 7.11–7.06 (m, 2H), 7.00 (t, J = 7.3 Hz, 1H), 5.92 (s, 1H), 3.47 (s, 3H), 3.41 (s, 4H), 2.34 (s, 4H); ^{13}C NMR (125 MHz, DMSO-d_6): δ 169.7, 161.5, 157.1, 152.0, 138.7, 138.0, 137.1, 133.0, 129.3, 129.2, 128.7, 128.7, 127.5, 123.3, 122.8, 120.8, 119.6, 118.7, 113.0, 96.6, 91.8, 62.2, 52.3 44.0; HRMS (ESI): *m/z* calculated for $C_{29}H_{29}N_8O_2S$ 553.2134 found 553.2152 [M+H] $^{+}$.

*8.1.2.16 1-(4-((1H-Indol-3-yl)thio)-6-(4-(pyridin-2-yl)piperazin-1-yl)pyrimidin-2-yl)-3-(4-chloro-2-methylphenyl)urea (**12p**)*

Off-white solid; yield 73%; mp:187-191 ^{o}C; FT-IR (cm^{-1}): 3368, 3212, 2931, 2611, 1869, 1739, 1738, 1675, 1385, 795; ^{1}H NMR (500 MHz, DMSO-d_6): δ 11.80 (s, 1H), 11.26 (s, 1H), 9.63 (s, 1H), 8.11 (d, J = 6.1 Hz, 1H), 7.85 (s, 1H), 7.59 (s, 1H), 7.53 (d, J = 6.9 Hz, 1H), 7.49 (d, J = 8.2 Hz, 1H), 7.45 (d, J = 7.9 Hz, 1H), 7.21 (dd, J = 14.9, 7.8 Hz, 2H), 7.11 (t, J = 7.8 Hz, 1H), 6.81 (d, J = 8.6 Hz, 1H), 6.68–6.63 (m, 1H), 6.58 (d, J = 6.2 Hz, 1H), 5.96 (s, 1H), 3.54 (s, 8H), 2.28 (s, 3H); ^{13}C NMR (125 MHz, DMSO-d_6): 169.8, 161.5, 158.9, 157.0, 152.0, 148.0, 137.9, 137.1, 133.5, 133.1, 131.5, 129.8, 128.8, 122.8, 120.8, 119.7, 118.7, 118.3, 113.6, 113.0, 107.5, 96.5, 91.8, 44.1, 43.5, 19.3; HRMS (ESI): *m/z* calculated for $C_{29}H_{28}ClN_8OS$ 571.1795 found 571.1799 [M+H] $^{+}$.

*8.1.2.17 1-(4-((1H-Indol-3-yl)thio)-6-(4-benzylpiperazin-1-yl)pyrimidin-2-yl)-3-phenylurea (**12q**)*

Off-white solid; yield 73%; mp:189-193 ^{o}C; FT-IR (cm^{-1}): 3358, 3102, 2986, 2611, 1879, 1563, 1384, 1175, 785; ^{1}H NMR (500 MHz, DMSO-d_6): δ 11.79 (s, 1H), 11.19 (s, 1H), 9.55 (s, 1H), 8.89 (s, 1H), 7.83 (d, J = 2.1 Hz, 1H), 7.46 (dd, J = 15.9, 7.6 Hz, 3H), 7.34–7.27 (m, 6H), 7.18 (t, J = 7.4 Hz, 1H), 7.10 (t, J = 7.4 Hz, 1H), 6.96 (d, J = 8.5 Hz, 2H), 6.03 (s, 1H), 3.61–3.33 (m, 6H), 2.35 (s, 4H); ^{13}C NMR (125 MHz, DMSO-d_6): δ 169.3, 161.1, 158.5, 156.5, 151.5, 147.5, 137.5, 136.7, 133.0, 132.6, 131.1, 129.3, 128.3, 122.3, 120.3, 119.2, 118.3, 117.8, 113.1, 112.6, 107.1, 96.0, 91.3, 43.7, 43.0; HRMS (ESI): *m/z* calculated for $C_{30}H_{30}N_7OS$ 536.2233 found 536.2251 [M+H] $^{+}$.

*8.1.2.18 1-(4-((1H-Indol-3-yl)thio)-6-(4-benzylpiperazin-1-yl)pyrimidin-2-yl)-3-(3,5-dimethylphenyl)urea (**12r**)*

Light brown solid; yield 78%; mp: 188-191 ^{o}C; FT-IR (cm^{-1}): 3367, 3114, 2898, 2609, 1859, 1563, 1394, 1275, 785; ^{1}H NMR (500 MHz, DMSO-d_6): δ 11.44 (s, 1H), 9.93 (s, 1H), 9.28 (s, 1H), 8.12 (s, 1H), 7.69 (s, 1H), 7.55 (t, J = 6.9 Hz, 1H), 7.38 (d, J = 8.1 Hz, 1H), 7.04 (d, J = 10.7 Hz, 2H), 7.02–6.90 (m, 5H), 6.85 (d, J = 8.6 Hz, 1H), 6.70–6.63 (m, 1H), 6.22 (s, 1H), 3.58 (d, J = 33.6 Hz, 10H), 1.86 (s, 6H); ^{13}C NMR (125 MHz, DMSO-d_6): δ 169.8, 161.5, 158.9, 157.0, 152.0, 148.0, 137.9, 137.1, 133.5, 133.1, 131.5, 129.8, 128.8, 122.8, 120.8, 119.7, 118.7, 118.3, 113.6, 113.0, 107.6, 96.5, 91.8, 44.1, 43.5, 19.3; HRMS (ESI): *m/z* calculated for $C_{32}H_{34}N_7OS$ 564.2546 found 564.2556 [M+H] $^{+}$.

*8.1.2.19 1-(4-((1H-Indol-3-yl)thio)-6-(4-benzylpiperazin-1-yl)pyrimidin-2-yl)-3-(4-chloro-2-methylphenyl)urea (**12s**)*

Light brown solid; yield 72%; mp: 183-187 ^{o}C; FT-IR (cm^{-1}): 3368, 3112, 2920, 2651, 1851, 1556, 1389, 1285, 760; ^{1}H NMR (500 MHz, DMSO-d_6): δ 11.78 (s, 1H), 11.23 (s, 1H), 9.58 (s, 1H), 7.83 (s, 1H), 7.54 (s, 1H), 7.47 (d, J = 8.1 Hz, 1H), 7.43 (d, J = 7.9 Hz, 1H), 7.34–7.25 (m, 5H), 7.18 (t, J = 8.9 Hz, 2H), 7.10 (t, J = 7.4 Hz, 1H), 6.55 (d, J = 8.2 Hz, 1H), 5.91 (s, 1H), 3.47 (s, 2H), 3.40 (s, 4H), 2.33 (s, 4H), 2.26 (s, 3H); ^{13}C NMR (125 MHz, DMSO-d_6): δ 169.7, 161.4, 157.0, 152.0, 138.1, 137.9, 137.1, 133.5, 133.0, 131.5, 129.8, 129.3, 128.7, 127.4, 122.8, 120.8, 119.6, 118.7, 118.2, 113.0, 96.5, 91.8, 62.2, 52.3, 43.9, 19.3; HRMS (ESI): *m/z* calculated for $C_{31}H_{31}ClN_7OS$ 583.1999 found 583.2011 [M+H] $^{+}$.

*8.1.2.20 1-(4-((1H-Indol-3-yl)thio)-6-(4-benzylpiperazin-1-yl)pyrimidin-2-yl)-3-(4-methoxyphenyl)urea (**12t**)*

White solid; yield 88%; mp: 192-196 ^{o}C; FT-IR (cm^{-1}): 3346, 3119, 2986, 1689, 1654, 1527, 1203, 875; ^{1}H NMR (500 MHz, DMSO-d_6): δ 11.77 (d, J = 1.9 Hz, 1H), 10.91 (s, 1H), 9.37 (s, 1H), 7.81 (d, J = 2.7 Hz, 1H), 7.44 (dd, J = 12.8, 8.0 Hz, 2H), 7.37–7.24 (m, 5H), 7.17 (dd, J = 11.0, 3.9 Hz, 1H), 7.10 (t, J = 7.5 Hz, 1H), 6.88 (dd, J = 23.0, 7.2 Hz, 2H), 6.81 (d, J = 9.0 Hz, 2H), 5.97 (s, 1H), 3.72 (d, J = 5.4 Hz, 3H), 3.57–3.34 (m, 6H), 2.34 (s, 4H); ^{13}C NMR (125 MHz, DMSO-d_6): δ 169.7, 161.1, 157.2, 155.5, 154.8, 152.1, 137.1, 133.4, 133.1, 131.8,

128.8, 122.7, 121.2, 120.7, 120.4, 118.7, 114.4, 113.0, 96.8, 91.4, 66.8, 55.6, 45.1; HRMS (ESI): *m/z* calculated for $C_{31}H_{32}N_7O_2S$ 566.2338 found 566.2342 $[M+H]^+$.

*8.1.2.21 1-(4-((1H-Indol-3-yl)thio)-6-(cyclopropylamino)pyrimidin-2-yl)-3-(4-chloro-2-methylphenyl)urea (**12u**)*

Off-white solid; yield 85%; mp: 190-195 ^oC; FT-IR (cm^{-1}): 3369, 3285, 2981, 1695, 1656, 1635, 1253, 831; ^1H NMR (500 MHz, DMSO-d_6): δ 12.61 (s, 1H), 12.31 (s, 1H), 10.43 (s, 1H), 8.58 (d, J = 46.6 Hz, 3H), 8.29 (d, J = 27.4 Hz, 3H), 8.04 (s, 2H), 7.94 (s, 2H), 3.53 (m, 1H), 3.08 (s, 3H), 1.50–0.84 (m, 4H); ^{13}C NMR (125 MHz, DMSO-d_6): δ 163.0, 156.9, 152.3, 138.3, 137.2, 133.5, 131.6, 129.8, 122.7, 120.8, 120.0, 118.7, 112.9, 19.3, 6.6; HRMS (ESI): *m/z* calculated for $C_{23}H_{22}ClN_6OS$ 465.1264 found 465.1282 $[M+H]^+$.

*8.1.2.22 1-(4-((1H-Indol-3-yl)thio)-6-(cyclopropylamino)pyrimidin-2-yl)-3-phenylurea (**12v**)*

Off-white solid; yield 78%; mp: 198-202 ^oC; FT-IR (cm^{-1}): 3367, 3151, 2891, 1692, 1675, 1643, 1425, 955; ^1H NMR (500 MHz, DMSO-d_6): δ 12.12 (s, 2H), 9.84 (s, 1H), 8.13 (s, 1H), 7.93 (s, 1H), 7.80 (dd, J = 23.9, 7.7 Hz, 4H), 7.61 (t, J = 7.0 Hz, 2H), 7.53 (t, J = 7.1 Hz, 1H), 7.45 (t, J = 7.0 Hz, 1H), 7.34 (t, J = 6.7 Hz, 1H), 5.80 (d, J = 145.1 Hz, 1H), 3.05 (s, 1H), 0.96–0.43 (m, 4H); ^{13}C NMR (125 MHz, DMSO-d_6): δ 163.0, 157.0, 152.3, 139.0, 137.2, 129.1, 128.8, 123.3, 122.7, 120.8, 120.0, 112.9, 96.9, 14.5, 6.7; HRMS (ESI): *m/z* calculated for $C_{22}H_{21}N_6OS$ 417.1498 found 417.1521 $[M+H]^+$.

*8.1.2.23 1-(4-((1H-Indol-3-yl)thio)-6-(phenylamino)pyrimidin-2-yl)-3-(p-tolyl)urea (**12w**)*

White solid; yield 86%; mp: 196-199 ^oC; FT-IR (cm^{-1}): 3368, 3112, 2889, 1698, 1675, 1638, 1412, 890; ^1H NMR (500 MHz, DMSO-d_6): δ 11.87 (s, 1H), 11.44 (s, 1H), 9.90 (s, 1H), 9.46 (s, 1H), 7.87 (s, 1H), 7.59–7.39 (m, 5H), 7.38–7.07 (m, 6H), 7.01 (t, J = 6.8 Hz, 1H), 6.90 (s, 1H), 5.70 (s, 1H), 2.27 (s, 3H); ^{13}C NMR (125 MHz, DMSO-d_6): δ 160.3, 156.9, 152.1, 139.4, 138.1, 137.2, 133.5, 131.5, 129.8, 129.3, 128.8, 123.7, 122.9, 121.4, 121.0, 119.5, 118.7, 118.3, 113.0, 96.4, 19.3; HRMS (ESI): *m/z* calculated for $C_{26}H_{23}N_6OS$ 467.1654 found 467.1663

*8.1.2.24 1-(4-((1H-Indol-3-yl)thio)-6-(phenylamino)pyrimidin-2-yl)-3-(4-chloro-2-methylphenyl)urea (**12x**)*

White solid; yield 82%; mp: 198-205 ^{o}C; FT-IR (cm^{-1}): 3366, 3207, 2926, 1696, 1685, 1587, 1253, 875; ^{1}H NMR (500 MHz, DMSO-d_6): δ 11.78 (s, 1H), 11.35 (s, 1H), 9.81 (s, 1H), 9.37 (s, 1H), 7.78 (s, 1H), 7.45 (t, J = 8.2 Hz, 3H), 7.35 (s, 2H), 7.19–7.12 (m, 2H), 7.11 (dd, J = 16.9, 8.0 Hz, 4H), 6.92 (t, J = 6.8 Hz, 1H), 5.61 (s, 1H), 2.19 (s, 3H); ^{13}C NMR (125 MHz, DMSO-d_6): δ 159.5, 156.1, 151.3, 138.6, 137.3, 136.5, 132.8, 130.7, 129.0, 128.6, 128.1, 122.9, 122.1, 120.7, 120.2, 118.7, 117.9, 117.5, 112.2, 95.6, 18.5; HRMS (ESI): *m/z* calculated for $C_{26}H_{22}ClN_6OS$ 501.1264 found 501.1276 [M+H] $^{+}$.

*8.1.2.25 1-(4-((1H-Indol-3-yl)thio)-6-((3,5-dimethoxyphenyl)amino)pyrimidin-2-yl)-3-(3,5-dimethoxyphenyl)urea (**12y**)*

White solid; yield 85%; mp: 199-202 ^{o}C; FT-IR (cm^{-1}): 3274, 2967, 2881, 1732, 1702, 1609, 1495, 755; ^{1}H NMR (500 MHz, DMSO-d_6): δ 11.78 (s, 1H), 10.93 (s, 1H), 9.42 (s, 1H), 8.36 (s, 1H), 7.83 (s, 1H), 7.46 (d, J = 3.8 Hz, 1H), 7.35 (d, J = 8.5 Hz, 2H), 7.19 (t, J = 7.4 Hz, 1H), 7.11 (t, J = 7.3 Hz, 1H), 6.94 (d, J = 8.5 Hz, 1H), 6.87–6.83 (m, 4H), 5.97 (s, 1H), 3.73 (d, J = 7.3 Hz, 6H), 3.59 (s, 3H), 3.39 (s, 3H); ^{13}C NMR (125 MHz, DMSO-d_6): δ 169.7, 161.8, 157.1, 155.5, 154.7, 153.4, 152.1, 137.1, 133.4, 133.1, 131.7, 128.8, 122.8, 121.3, 120.8, 120.3, 118.7, 114.3, 113.0, 96.5, 91.6, 55.6; HRMS (ESI): *m/z* calculated for $C_{29}H_{29}N_6O_5S$ 573.1920 found 573.1936 [M+H] $^{+}$.

*8.1.2.26 1-(4-((1H-Indol-3-yl)thio)-6-((3,5-dimethoxyphenyl)amino)pyrimidin-2-yl)-3-(4-methoxyphenyl)urea (**12z**)*

White solid; yield 79%; mp: 200-206 ^{o}C; FT-IR (cm^{-1}): 3364, 3151, 2881, 1685, 1646, 1527, 1418, 813; ^{1}H NMR (500 MHz, DMSO-d_6): δ 11.71 (s, 1H), 10.86 (s, 1H), 9.35 (s, 1H), 8.30 (s, 1H), 7.76 (s, 1H), 7.39 (dd, J = 12.1, 8.2 Hz, 2H), 7.28 (d, J = 8.5 Hz, 3H), 7.13 (t, J = 7.4 Hz, 1H), 7.04 (t, J = 7.3 Hz, 1H), 6.88 (d, J = 8.5 Hz, 1H), 6.78 (d, J = 7.3 Hz, 3H), 5.90 (s, 1H), 3.66 (d, J = 7.3 Hz, 6H), 3.52 (s, 3H); ^{13}C NMR (125 MHz, DMSO-d_6): δ 168.7, 160.7, 156.0, 154.4, 153.7, 152.3, 151.0, 136.1, 132.3, 132.1, 130.6, 127.8, 121.7, 120.2, 119.7, 119.3, 117.6, 113.3, 111.9, 95.4, 90.6, 54.5; HRMS (ESI): *m/z* calculated for $C_{28}H_{27}N_6O_4S$ 543.1814 found 543.1826 [M+H] $^{+}$.

*8.1.2.27 1-(4-((1H-Indol-3-yl)thio)-6-((4-chloro-phenyl)amino)pyrimidin-2-yl)-3-phenylurea (**12aa**)*

White solid; yield 76%; mp: 200-206 ^{o}C; FT-IR (cm^{-1}): 3364, 3151, 2881, 1685, 1646, 1527, 1418, 813; ^{1}H NMR (500 MHz, DMSO-d_6): δ 11.88 (d, J = 1.8 Hz, 1H), 11.42 (s, 1H), 10.04 (s, 1H), 9.55 (s, 1H), 7.94 (d, J = 4.7 Hz, 1H), 7.88 (d, J = 2.7 Hz, 1H), 7.54 (t, J = 7.9 Hz, 2H), 7.48 (d, J = 8.1 Hz, 1H), 7.34–7.24 (m, 4H), 7.30–7.13 (m, 4H), 7.05 (dd, J = 8.5, 5.7 Hz, 1H), 5.70 (s, 1H); ^{13}C NMR (125 MHz, DMSO-d_6): δ 169.8, 161.5, 158.9, 157.0, 152.0, 148.0, 137.9, 137.1, 133.5, 133.1, 131.5, 129.8, 128.8, 122.8, 120.8, 119.7, 118.7, 118.3, 113.6, 113.0, 107.5, 96.5, 91.8; HRMS (ESI): *m/z* calculated for $C_{25}H_{20}ClN_6OS$ 487.1108 found 487.1116 $[M+H]^+$.

8.2 Pharmacology

8.2.1 Cell culture

Prostate (PC-3), lung (A549), Breast (MDAMB-231) and Liver (HepG2) cells were purchased from ATCC. PC-3 and A549 cells were grown in RPMI medium whereas MDAMB-231, HepG2 were maintained in DMEM supplemented with 10% fetal bovine serum (FBS) and 1% penicillin-streptomycin (PS). All the cell lines were grown in an incubator with 75% humidity and 5% CO_2 at 37 ºC. 0.25% trypsin-ethylenediaminetetraacetic acid (EDTA, Life Technologies) was used for harvesting the cells. For all the assays, stock solutions of the compounds were prepared in DMSO (10 mM).

8.2.2 Evaluation of in vitro cytotoxic effects

In this assay, Prostate (PC-3), lung (A549), Breast (MDA-MB-231) and Liver (HepG2) cells were seeded in 96 well plates depending on their doubling time and were grown overnight. The cells were exposed to different concentrations of carbamide derivatives of indole-pyrimidine conjugates **12a-aa** (100, 10, 1, 0.1 and 0.01 μM) for 72 h. Then, the medium containing compounds was removed and replaced with 100 μL of MTT solution (5 mg/mL) and the cells were further incubated for 4 h in dark at 37 ºC. The unreacted MTT solution was removed and 100 μL DMSO was added to each well to solubilize the produced formazan crystals. The absorbance of the purple formazan solution was recorded using a plate reader (SpectraMax) at 570 nm and the IC_{50} values for each compound were calculated. All the experiments were repeated three times and the standard deviations are reported in **Table 1**.

8.2.3 In-Vitro VEGFR-2 inhibition assay

The VEGFR-2 tyrosine kinase activity of the compounds was performed according to BPS Bioscience Corporation, San Diego, CA, USA (www.bpsbioscience.com) protocol, where VEGFR-2 (KDR) (BPS#40301) served as the enzyme source and Poly (Glu, Tyr) sodium salt, (4:1, Glu:Tyr) (Sigma#P7244) served as the standardized substrate and Kinase Glo Plus Luminescence kinase assay kit (Promega#V3772) [46]. In this assay, 5 μL of the compounds **12a-aa** (1 nM, 10 nM, 100 nM, 1 μM, 10 μM) was added to a 45 μL of reaction mixture (40 mM Tris, pH 7.4, 10 mM $MgCl_2$, 0.1 mg/mL BSA, 1 mM DTT, 10 μM ATP, Kinase substrate and VEGFR-2) and incubated at 30 ºC for 45 min. After the enzymatic reaction, 50 μL of Kinase-Glo Plus Luminescence kinase assay solution (Promega) was added to each reaction well and the plate was further incubated for 15 min at room temperature in dark [47]. The luminescent signal was measured using a microplate reader (SpectraMax). The intensity of the ATP luminescence is inversely proportional to the amount of kinase activity. The assays were performed in triplicate for each concentration and the IC_{50} values were determined from non-linear regression analysis of the sigmoidal dose-response curve generated in Graph pad prism.

8.2.4 Molecular docking

The molecular docking studies were performed at the AXI binding site of VEGFR-2 (PDB ID: 3WZE). The coordinates of the crystal structure were obtained from RCSB-Protein Data Bank and suitable corrections were made using Protein Preparation Wizard from the Schrodinger package. Regarding the ligands, molecules were constructed using ChemBio3D Ultra 12.0 and their geometries were optimized using molecular mechanics. Finally, docking studies were performed according to the standard protocol implemented in maestro software, version 9.9 on the most active molecules [48]. The ligand-protein complex was analyzed for interactions and 3D pose of most active compound **12k** was imaged using Schrödinger. In this research, in order to further investigate the antiproliferative activity of target compounds against VEGFR-2, the in vitro antiproliferative activity data of VEGFR-2 were chose to construct the 3D-Quantitative Structure Activity Relationship (3D-QSAR) models. **Table 6** listed the structures of all target compounds and the IC_{50} values against VEGFR-2. Field and atom-based analysis were performed using IC_{50} values for all target compounds against VEGFR-2. Then, the IC50 values were converted to pIC50 values according to the following formula: pIC_{50} = Ig $1/IC_{50.}$ Construction of all target compounds, structural optimization, and 3D-QSAR modeling were all performed on maestro software, version 9.9.

8.2.5 HUVECs tube formation assay

BD Matrigel™ (BD Bio-science, Heidelberg Germany) was thawed at 4 ^{o}C overnight prior to the coating of matrigel in a 96 well plate. The plates were placed on ice prior to the coating and 50 µL of matrigel was slowly added to each well with constant, gentle agitation for an even layer formation. The coated plates were incubated at 37 ºC in a 5% CO_2 atmosphere for 1 h. The gels were overlaid with cells (10000 HUVEC cells/well) in M200 media containing either the vehicle (0.3% DMSO) or the synthesized compound **12k**. The plates were visualized for live cells with the aid of calcein-AM (4 M) after 16 h of incubation. The image for both the bright field and green channels were recorded using an inverted microscope (BIORAD) to observe the subsequent effect of the compounds on the tubular structure formation.

8.2.6 Cell Invasion/Transwell assay

The invasion ability of HUVEC cells was assessed using transwell chambers with polycarbonate filters. HUVEC cells starved with serum for 24 h were collected and resuspended in medium contain 0.1% FBS. The cells were seeded in the transwells with 8 µm pores (20000 cells/well in 0.2 mL) and were inserted in the 24 well plate. To the lower chamber of the plate was added 10% FBS as chemoattractant. Cells were treated with the compound **12k**. After incubation, the cells remaining on the upper side of the transwell chamber were swabbed with a cotton tip and the cells that migrated to the lower chamber were fixed with methanol and stained with crystal violet. The images were captured using an inverted fluorescence microscope (Nikon).

8.2.7 Colony Forming Assay

MDA-MB-231 cells in exponential growth phase were seeded into 6-well plates at 4000 cells/well. After 24 h incubation, the culture medium was replaced with medium containing increasing concentrations (1, 3 and 5 µM) of compound **12k** and 1% DMSO (control). The cells were incubated for 7 days and the drug-containing medium was replenished after 3 days. Each treatment was performed in triplicate. After incubation, the cells were washed twice with PBS, fixed with 4% paraformaldehyde for 20 min and stained with crystal violet for a further 15 min. Scans of 6-well plates were generated on an Epson.

8.2.8 Wound healing assay (migration assay)

Confluent MDA-MB-231 monolayers in 30 mm petri dishes were wounded with 200 μL pipette tips, giving rise to 1 mm wide lanes per well. The cell debris was removed by washing with PBS and cells were supplied with 2 mL of complete medium (controls) or complete medium containing different concentrations compound **12k** (b & c) and sorafenib (d & e). The wounds were observed by phase contrast microscopy immediately and after 24 h incubation.

8.2.9 Identification of apoptotic cells

Changes in the nuclear morphology of MDA-MB-231cells were determined using Hoechst 33342. In this assay, MDA-MB-231 cells were grown on cover slips in a 6-well plate at a density of $1X10^6$ cells/well and were incubated with different concentrations of compounds **12e** and **12k** for 48 h. The cells were washed with PBS and 4% paraformaldehyde solution was added. The cells were incubated with 2 μg/mL Hoechst 33242 for 20 minutes then washed three times with PBS to remove excess dye. The morphological changes in the nuclei were observed using a ZOE™ Fluorescent Cell Imager (BIO-RAD).

8.2.10 Quantification of apoptotic cells

MDA-MB-231 cells ($1x10^6$/well) were grown in 6 well plate and treated with increasing concentrations of compound **12k** for 48 h. After incubation, the cells were trypsinised and washed with PBS. The obtained cell pellet was resuspended in 1x annexin binding buffer. 5 μL of annexin V and 1 μL of PI was added to the resuspended cells and incubated for 15 min at room temp. 10000 cells from each sample were used for analysis using a BD Accuri C6 flow cytometer.

8.2.11 Effect on mitochondrial membrane potential

MDA-MB-231 Cells were grown in 24-well plates ($5x10^5$ cells/mL) and incubated with different concentrations (2.5 and 5 μM) of compounds **12e** and **12k**. After 48 h incubation, the medium containing the compound was replaced with 500 μL of fresh medium containing 5 μg/mL JC-1 and further incubated for 20 min. The cells were washed three times with PBS to remove excess dye and photographed in red and green channels using a ZOE™ Fluorescent Cell Imager (BIO-RAD).

8.2.12 Effect on intracellular ROS generation

The intracellular ROS levels in MDA-MB-231 cells were determined by carboxy-H_2DCFDA staining. In this assay, MDA-MB-231 cells were incubated with increasing concentrations of compounds **12e** and **12k** (2.5 and 5 μM) for 48 h. After incubation, the cells were harvested and stained with a 10 μM solution of carboxy-H_2DCFDA in PBS for 20 min at 37 ºC. The intensity of the green fluorescence was analyzed using ZOE™ Fluorescent Cell Imager (BIO-RAD).

Acknowledgments

SS and RT are thankful to DoP, Ministry of Chemicals & Fertilizers, Govt. of India, New Delhi, for the award of NIPER fellowship. The authors acknowledge the Micro Nano Research Facility (MNRF), RMIT University, for providing the facilities to carry out cell culture experiments.

References

1. J. Holenz, D. G. Brown, Modern lead generation strategies. In Lead Generation: Methods and Strategies; J. Holenz, R. Mannhold, H. Kubinyi, G. Folkers, Eds, Wiley-VCH Verlag GmbH & Co. KGaA: Weinheim, Germany, (2016) 13-33; b) J. R. Morphy, Historical strategies for lead generation. RSC Drug Discovery 21 (2012) 111-129.

2. a) D. G. Brown, J. Boström, Where Do Recent Small Molecule Clinical Development Candidates Come From? J. Med. Chem. 61 (2018) 9442-9468; b) J. Boström, A. Hogner, S. Schmitt, Do structurally similar molecules bind in a similar fashion? J. Med. Chem. 49 (2006) 6716-6725.

3. a) W.-S. Huang, S. Liu, D. Zou, M. Thomas, Y. Wang, T. Zhou, J. Romero, A. Kohlmann, F. Li, J. Qi, L. Cai, T. A. Dwight, Y. Xu, R. Xu, R. Dodd, A. Toms, L. Parillon, X. Lu, R. Anjum, S. Zhang, F. Wang, J. Keats, S. D. Wardwell, Y. Ning, Q. Xu, L. E. Moran, Q. K. Mohemmad, H. G. Jang, T. Clackson, N. I. Narasimhan, V. M. Rivera, X. Zhu, D. Dalgarno, W. C. Shakespeare, Discovery of brigatinib (AP26113), a phosphine oxide-containing, potent, orally active inhibitor of anaplastic lymphoma kinase. J. Med. Chem. 59 (2016) 4948-4964; b) R. H. Bradbury, R. Callis, G. R. Carr, H. Chen, E. Clark, L. Feron, S. Glossop, M. A. Graham, M. Hattersley, C. Jones, S. G. Lamont, G. Ouvry, A. Patel, J. Patel, A. A. Rabow, C. A. Roberts, S. Stokes, N. Stratton, G. E. Walker, L. Ward, D. Whalley, D. Whittaker, G. Wrigley, M. J. Waring, Optimization of a series of bivalent triazolopyridazine

based bromodomain and extraterminal inhibitors: the discovery of (*3R*)-4-[2-[4-[1-(3-methoxy-[1,2,4]-triazolo[4,3-b]pyridazin-6-yl)-4-piperidyl]phenoxy] ethyl]-1,3-dimethyl-piperazin-2-one (AZD5153). J. Med. Chem. 59 (2016) 7801-7817; c) F. Beaufils, N. Cmiljanovic, V. Cmiljanovic, T. Bohnacker, A. Melone, R. Marone, E. Jackson, X. Zhang, A. Sele, C. Borsari, J. Mestan, P. Hebeisen, P. Hillmann, B. Giese, M. Zvelebil, D. Fabbro, R. L. Williams, D. Rageot, M. P. Wymann, 5-(4,6-Dimorpholino- 1,3,5-triazin-2-yl)-4-(trifluoromethyl)pyridin-2-amine (PQR309), a potent, brain-penetrant, orally bioavailable, pan-class I PI3K/mTOR inhibitor as clinical candidate in oncology. J. Med. Chem. 60 (2017) 7524-7538.

4. a) S. Nekkanti, O. Ommi , P. S. S. Lakshmi, N. Shankaraiah, Diverse targeted approaches to battle multidrug resistance in cancer, 26 (2019) 7059-7080. b) N. Shankaraiah, A. P. Sakla, K. Laxmikeshav, R. Tokala, Reliability of Click Chemistry on Drug Discovery: A Personal Account, 19 (2019) 1-21. c) A. Kamal, S. Nekkanti, N. Shankaraiah, S. Manda, Future of Drug Discovery: Drug Resistance in Bacteria, Fungi, Malaria, and Cancer, Eds, Springer International Publishing, (2017) 609-629.

5. a) I. Zuazo-Gaztelu, O. Casanovas, Unraveling the Role of Angiogenesis in Cancer ecosystems, Front. Oncol. 8 (2018) 248; b) Z. K. Otrock, R. A. R. Mahfouz, J. A. Makarem, A. I. Shamseddine, Understanding the biology of angiogenesis: Review of the most important molecular mechanisms, Blood Cells, Molecules, and Diseases 39 (2007) 212–220; c) A. Markowska, S. Sajdak, J. Markowska, A. Huczynski, Angiogenesis and cancer stem cells: New perspectives on therapy of ovarian cancer, Eur. J. Med. Chem. 142 (2017) 87-94.

6. a) M. Potente, H. Gerhardt, P. Carmeliet, Basic and therapeutic aspects of angiogenesis. Cell 146 (2011) 873-887; b) L. Yadav, N. Puri, V. Rastogi, P. Satpute, V. Sharma, Tumour Angiogenesis and Angiogenic Inhibitors: A Review; J. Clin. Diagn. Res. 9 (2015) XE01-XE05; c) K. Zirlika, J. Duyster, Anti-Angiogenics: current Situation and future perspectives, Oncol. Res. Treat. 41 (2018) 166–171.

7. a) C. Fontanella, E. Ongaro, S. Bolzonello, M. Guardascione, G. Fasola, G. Aprile Clinical advances in the development of novel VEGFR2 inhibitors, Ann. Transl. Med. 2 (2014) 123; b) S. Koch, L. Claesson-Welsh, Signal transduction by vascular endothelial growth factor receptors Biochem. J. 437 (2011) 169-83; c) S. P. Ivy, J. Y. Wick, B. M. Kaufman, An

overview of small molecule inhibitors of VEGFR signalling. Nat. Rev. Clin. Oncol. 6 (2009) 569-579.

8. a) F. Musumeci, M. Radi, C. Brullo, S. Schenone, Vascular Endothelial Growth Factor (VEGF) receptors: Drugs and new Inhibitors, J. Med. Chem. 55 (2012) 10797-10822; b) S. J. Modi, V. M. Kulkarni, Vascular Endothelial Growth Factor Receptor (VEGFR-2)/KDR Inhibitors: Medicinal Chemistry Perspective, Medicine in Drug Discovery 2 (2019) 100009; c) F. W. Peng, D. K. Liu, Q. W. Zhang, Y. G. Xu, L. Shi, VEGFR-2 inhibitors and the therapeutic applications thereof: a patent review (2012-2016), Expert Opin. Ther. Pat. 27(2017) 987-1004.

9. a) S. Kumar, B. Narasimhan, Therapeutic potential of heterocyclic pyrimidine scaffolds, Kumar S, Narasimhan B. Therapeutic potential of heterocyclic pyrimidine scaffolds. Chem. Cent. J. 12 (2018) 38; b) H. Dansena, H. J. Dhongade, K. Chandrakar, Pharmacological Potentials of Pyrimidine Derivative: A Review, Asian J. Pharm. Clin. Res. 8 (2015) 171-177; c) T. P. Selvam, C. R. James, P. V. Dniandev, S. K. Valzita, Research in Pharmacy 2 (2012) 01-09.

10. a) P. C. Diao, W. Y. Lin, X. E. Jian, Y. H. Li, W. W. You, P. L. Zhao, Discovery of novel pyrimidine-based benzothiazole derivatives as potent cyclin-dependent kinase 2 inhibitors with anticancer activity, Eur. J. Med. Chem. 179 (2019) 196-207; b) C. S. Munikrishnappa, S. B. Puranik, G.V. S. Kumar, Y. R. Prasad, Part-1: Design, synthesis and biological evaluation of novel bromopyrimidine analogs as tyrosine kinase inhibitors, Eur. J. Med. Chem. 119 (2016) 70-82.

11. a) M. Zhu, L. Ma, H. Zhou, B, Dong, Y. Wang, Z. Wang, J. Zhou, G. Zhang, J. Wang, C. Liang, S. Cen, Y. Wang, Preliminary SAR and biological evaluation of potent HIV-1 protease inhibitors with pyrimidine bases as novel P2 ligands to enhance activity against DRV-resistant HIV-1 variants, Eur. J. Med. Chem. 185 (2020) 111866; b) M. H. Mehraban, R. Yousefi, A. T. Kafrani, F. Panahi, A. Nezhad, Binding study of novel anti-diabetic pyrimidine fused heterocycles to β-lactoglobulin as a carrier protein, Colloids Surf B Biointerfaces. 112 (2013) 374-379.

12. A. M. Farghaly, O. M. AboulWafa, Y. A. M. Elshaier, W. A. Badawi, H. H. Haridy, H. A. E. Mubarak, Design, synthesis, and antihypertensive activity of new pyrimidine derivatives

endowing new pharmacophores, Med. Chem. Res. 28 (2019) 360–379; b) J. K. Gupta, P. K. Sharma, R. Dudhe, S. C. Mondal, A. Chaudhary, P. K. Verma, Synthesis and analgesic activity of novel pyrimidine derivatives of coumarin moiety, Acta Pol. Pharm. 68 (2011) 785-93; c) V. Kolman, F. Kalcic, P. Jansa, Z. Zídek, Z. Janeba, Influence of the C-5 substitution in polysubstituted pyrimidines on inhibition of prostaglandin E_2 production, Eur. J. Med. Chem. 156 (2018) 295-301.

13. a) P. Liu, Y. Yang, Y. Tang, T. Yang, Z. Sang, Z. Liu, T. Zhang, Y. Luo, Design and synthesis of novel pyrimidine derivatives as potent antitubercular agents, Eur. J. Med. Chem. 163 (2019) 169-182; b) S. Federico, E. Margiotta, V. Salmaso, G. Pastorin, S. Kachler, K. Klotz, S. Moro, G. Spalluto, [1,2,4] Triazolo [1,5-*c*] pyrimidines as adenosine receptor antagonists: Modifications at the 8 position to reach selectivity towards A_3 adenosine receptor subtype, Eur. J. Med. Chem. 157 (2018) 837-851; c) Z. Fang, S. Zheng, K.Chan, W. Yuan, Q. Guo, W. Wu, H. Lui, Y. Lu, Y. Leung, T. Chan, K. Wong, N. Sun, Design, synthesis and antibacterial evaluation of 2,4-disubstituted-6-thiophenyl-pyrimidines, Eur. J. Med. Chem. 161 (2019) 141-153.

14. a) R. Kaur, P. Kaur, S. Sharma, G. Singha, S. Mehndiratta, P. M. S. Bedia, K. Nepalia, Anti-Cancer Pyrimidines in Diverse Scaffolds: A Review of Patent Literature, Recent Pat. Anticancer Drug Discov. 10 (2015) 23-71; b) S. Chang, L. Zhang, S. Xu, J. Luo, X. Lu, Z. Zhang, T. Xu, Y. Liu, Z. Tu, Y. Xu, X. Ren, M. Geng, J. Ding, D. Pei, K. Ding, Design, synthesis, and biological evaluation of novel conformationally constrained inhibitors targeting epidermal growth factor receptor threonine790 → methionine790 mutant, J. Med. Chem. 55 (2012) 2711-2723; c) C. B. Barlaam, R. Ducray, G. J. Kettle, Pyrimidine derivatives 934.WO2009010789 (**2009**).

15. a) S. Mahboobi, S, Dove, A. Sellmer, M. Winkler, E. Eichhorn, H. Pongratz, T.Ciossek, T. Baer, T. Maier, T. Beckers, Design of chimeric histone deacetylase- and tyrosine kinase-inhibitors: a series of imatinib hybrids as potent inhibitors of wild-type and mutant bcr-abl, pdgf-rβ, and histone deacetylases, J. Med. Chem. 52 (2009) 2265-2279; b) J. E. Hawkinson, R. Sinville, D. Mudaliar, J. Shetty, T. Ward, J. C. Herr, G. I. Georg, Potent pyrimidine and pyrrolopyrimidine inhibitors of testis-specific serine/threonine kinase 2 (TSSK2), ChemMedChem. 12 (2017) 1857-1865.

16. a) S. A. Long, A. Thorarensen, M. E. Schnute, Pyrimidine and pyridine derivatives useful in therapy. WO2013054185 (2013).b) K. Geng, H. Liu, Z. Song, C. Zhang, M. Zhang, H. Yang, J. Cao, M. Geng, A. Shen, A. Zhang, Design, synthesis and pharmacological evaluation of ALK and Hsp90 dual inhibitors bearing resorcinol and 2,4-diaminopyrimidine motifs. Eur. J. Med. Chem. 152 (2018) 76-86; c) Pass, M. 2,4,6-Trisubstituted pyrimidines as phosphotidylinositol-3-kinase inhibitors and their use in the treatment of cancer. US20090143384 (**2009**).

17. a) P. A. Harris, A. Boloor, M. Cheung, R. Kumar, R. M. Crosby, R. G. Davis-Ward, A. H. Epperly, K. W. Hinkle, R. N. Hunter, J. H. Johnson, V. B. Knick, C. P. Laudeman, D. K. Luttrell, R. A. Mook, R. T. Nolte, S. K. Rudolph, J. R. Szewczyk, A. T. Truesdale, J. M. Veal, L. Wang, J. A. Stafford, Discovery of 5-[[4-[(2,3-dimethyl-2*H*-indazol-6-yl)methylamino]-2-pyrimidinyl]amino]-2-methyl-benzenesulfonamide (pazopanib), a novel and potent vascular endothelial growth factor receptor inhibitor. J. Med. Chem. 51 (2008) 4632−4640; b) R. M. Bukowski, U. Yasothan, P. Kirkpatrick, Pazopanib. Nat. Rev. Drug Discov., 9 (2010) 17−18.

18. R. L. Hudkins, N. C. Becknell, A. L. Zulli, T. L. Underiner, T. S. Angeles, L. D. Aimone, M. S. Albom, H. Chang, S. J. Miknyoczki, K. Hunter, S. Jones-Bolin, H. Zhao, E. R. Bacon, J. P. Mallamo, M. A. Ator, B. A. Ruggeri, Synthesis and biological profile of the pan-vascular endothelial growth factor receptor/tyrosine kinase with immunoglobulin and epidermal growth factor-like homology domains 2 (VEGF-R/TIE-2) inhibitor 11-(2-methylpropyl)-12,13-dihydro-2-methyl-8-(pyrimidin-2-ylamino)-4*H*-indazolo[5,4-*a*]pyrolo[3,4-*c*]-carbazol-4-one (CEP-11981): a novel oncology therapeutic agent. J. Med. Chem., 55 (2012) 903-913.

19. a) P. V. Thanikachalam, R. K. Maurya, V. Garg, V. Monga, An insight into the medicinal perspective of synthetic analogs of indole: A review, Eur. J. Med. Chem. 180 (2019) 562-612; b) Y. Wan, Y. Li, C. Yan, M. Yan, Z. Tang, Indole: A privileged scaffold for the design of anti-cancer agents, Eur. J. Med. Chem., 183 (2019) 111691.

20. a) J.-S. Shin, H.-E. Choi, S.-D. Kim, Y. S. Lee, Y.-W. Cho, K. T. Lee, Anti-inflammatory effects of 7-hydroxyl-1-methylindole-3-acetonitrile, a synthetic arvelexin derivative, on the macrophages through destabilizing mPGES-1 mRNA and suppressing NF-kB activation, Chem. Biol. Interact. 224 (2014) 68-77; b) M. S. Estevao, L. C. Carvalho, D. Ribeiro, D.

Couto, M. Freitas, A. Gomes, L. M. Ferreira, E. Fernandes, M. M. B. Marques, Antioxidant activity of unexplored indole derivatives: synthesis and screening, Eur. J. Med. Chem. 45 (2010) 4869-4878; c) P. Ashok, C.-L. Lu, S. Chander, Y.-T. Zheng, S. Murugesan, Design, synthesis, and biological evaluation of 1-(thiophen-2-yl)-9*H*-pyrido[3,4-*b*]indole derivatives as anti-HIV-1 agents, Chem. Biol. Drug Des. 85 (2015) 722-728.

21. a) S. B. Bharate, R. R. Yadav, S. I. Khan, B. L. Tekwani, M. R. Jacob, I. A. Khan, R. A. Vishwakarma, Meridianin G and its analogs as antimalarial agents, Medchemcomm 4 (2013) 1042-1048; b) K. Sharma, O. Tanwar, S. Sharma, S. Ali, M.M. Alam, M.S. Zaman, M. Akhter, Structural comparison of *Mtb*-DHFR and h-DHFR for design, synthesis and evaluation of selective non-pteridine analogues as antitubercular agents, Bioorg. Chem. 80 (2018) 319-333; c) T. L. Kerley, A. B. Richards, R. W. Begley, B. E. Abreu, L. C. Weaver, Anticonvulsant and antitremor effects of chlorphenoxamine, J. Pharmacol. Exp. Ther. 132 (1961) 360-365; d) M. Nazir, M. A. Abbasi, Aziz-ur-Rehman, S. Z. Siddiqui, K. M. Khan, Kanwal, U. Salar, M. Shahid, M. Ashraf, M. Arif Lodhi, F. Ali Khan, New indole based hybrid oxadiazole scaffolds with *N*-substituted acetamides: as potent antidiabetic agents, Bioorg. Chem. 81 (2018) 253-263.

22. a) C. Praveen, A. Ayyanar, P. T. Perumal, Practical synthesis, anticonvulsant, and antimicrobial activity of N-allyl and N-propargyl di(indolyl)indolin-2-ones, Bioorg. Med. Chem. Lett 21 (2011) 4072-4077; b) M.-Z. Zhang, C.-Y. Jia, Y.-C. Gu, N. Mulholland, S. Turner, D. Beattie, W.-H. Zhang, G.-F. Yang, J. Clough, Synthesis and antifungal activity of novel indole-replaced streptochlorin analogues, Eur. J. Med. Chem. 126 (2017) 669-674; c) S. Rajan, S. Puri, D. Kumar, M. H. Babu, K. Shankar, S. Varshney, A. Srivastava, A. Gupta, M. S. Reddy, A. N. Gaikwad, Novel indole and triazole based hybrid molecules exhibit potent anti-adipogenic and antidyslipidemic activity by activating Wnt3a/b-catenin pathway, Eur. J. Med. Chem. 143 (2018) 1345-1360.

23. a) C. R. Lindsay, I. R. MacPherson, J. Cassidy, Current status of cediranib: the rapid development of a novel anti-angiogenic therapy. Future Oncol. 5 (2009) 421−432; b) S. R. Alberts, T. R. Fitch, G. P. Kim, B. W. Morlan, S. R. Dakhil, H. M. Gross, S. Nair, Cediranib (AZD2171) in patients with advanced hepatocellular carcinoma: a phase II north central cancer treatment troup clinical trial. Am. J. Clin. Oncol. 35 (2012) 329-333; c) Z. W. Cai, Y.

Zhang, R. M. Borzilleri, L. Qian, S. Barbosa, D. Wei, X. Zheng, L. Wu, J. Fan, Z. Shi, B. S. Wautlet, S. Mortillo, R. Sr. Jeyaseelan, D. W. Kukralmgrt, A. Kamath, P. Marathe, C. D'Arienzo, G. Derbin, J. C. Barrish, J. A. Robl, J. T. Hunt, L. J. Lombardo, J. Fargnoli, R. S. Bhide, Discovery of brivanib alaninate ((*S*)-((*R*)-1-(4-(4-fluoro-2-methyl-1*H*-indol-5-yloxy)-5-methylpyrrolo[2,1-*f*][1,2,4]triazin-6-yloxy)propan-2-yl)2-aminopropanoate), a novel prodrug of dual vascular endothelial growth factor receptor-2 and fibroblast growth factor receptor-1 kinase inhibitor (BMS-540215). J. Med. Chem. 51 (2008) 1976-1980; d) R. S. Finn, Y. K. Kang, M. Mulcahy, B. N. Polite, H. Y. Lim, I. Walters, C. Baudelet, D. Manekas, J. W. Park, Phase II, open-label study of brivanib as second-line therapy in patients with advanced hepatocellular carcinoma. Clin. Cancer Res. 18 (2012) 2090-2098.

24. a) A. K. Ghosh, M. Brindisi, Urea Derivatives in Modern Drug Discovery and Medicinal Chemistry, J. Med. Chem. 2019, doi: 10.1021/acs.jmedchem.9b01541; b) J. R. Browna, E. J. Northa, J. G. Hurdle, C. Morisseau, J. S. Scarborough, D. Suna, J. Korduláková, M. S. Scherman, V. Jones, A. Grzegorzewicz, R. M. Crew, M. Jackson, M. R. McNeil, R. E. Lee, The structure activity relationship of urea derivatives as anti-tuberculosis agents, Bioorg. Med. Chem. 19 (2011) 5585-5595.

25. a) Q. W. Zhang, Y. Y. Diao, F. Wang, Y. Fu, F. Tang, Q. D. You, H. Y. Zhou, Design and discovery of 4-anilinoquinazoline ureas as multikinase inhibitors targeting BRAF, VEGFR-2 and EGFR, Med.Chem.Comm., 4 (2013) 979-986; b) A. Akhmanova, M. O. Steinmetz, Control of microtubule organization and dynamics: two ends in the limelight. Nat. Rev. Mol. Cell Biol. 16 (2015) 711-726.

26. a) S. Wilhelm, C. Carter, M. Lynch, T. Lowinger, J. Dumas, R. A. Smith, B. Schwartz, R. Simantov, S. Kelley, Discovery and development of sorafenib: a multikinase inhibitor for treating cancer. Nat. Rev. Drug Discov., (2006) 835-844; b) R. Gedaly, P. Angulo, C. Chen, K. T. Creasy, B. T. Spear, J. Hundley, M. F. Daily, M. Shah, B. M. Evers, The role of PI3K/mTOR inhibition in combination with sorafenib in hepatocellular carcinoma treatment. Anticancer Res. 32 (2012) 2531-2536.

27. a) S. M. Wilhelm, J. Dumas, L. Adnane, M. Lynch, C. A. Carter, G. Schütz, K. H. Thierauch, D. Zopf, Regorafenib (BAY 73-4506): a new oral multikinase inhibitor of angiogenic, stromal and oncogenic receptor tyrosine kinases with potent preclinical

antitumor activity. Int. J. Cancer 129 (2011) 245-255; b) C. Aversa, F. Leone, G. Zucchini, G. Serini, E. Geuna, A. Milani, D. Valdembri, R. Martinello, F. Montemurro, Linifanib: current status and future potential in cancer therapy. Expert Rev. Anticancer Ther. 15 (2015) 677-687.

28. a) D. R. Shepard, M. M. Cooney, P. Elson, R. M. Bukowski, R. Dreicer, B. I. Rini, J. A. Garcia, A phase II study of tandutinib (MLN518), a selective inhibitor of type III tyrosine receptor kinases, in patients with metastatic renal cell carcinoma. Invest. New Drugs 30 (2012) 364-367; b) https://www.clinicaltrials.gov/ct2/show/NCT02438761 (accessed Feb 18, 2020).

29. a) Y. Zhang, Y. Chen, D. Zhang, L. Wang, T. Lu, Y. Jiao, Discovery of Novel Potent VEGFR□2 Inhibitors Exerting Significant Antiproliferative Activity against Cancer Cell Lines, J. Med. Chem. 61 (2018) 140-157; b) L. Huang, Z. Huang, Z. Bai, R. Xie, L. Sun, K. Lin, Development and strategies of VEGFR-2/KDR inhibitors, Future Med. Chem. 4 (2012) 1839-1852.

30. a) T. Liljefors, I. Em. Petterson, A textbook of drug design and development; b) V. J. Claudio, D. Amanda, B. Vanderlan, B. Eliezer, F. C. Alberto, Molecular hybridization: a useful tool in the design of new drug prototypes, Cur. Med. Chem. 14 (2007) 1829-1852.

31. a) S. Sana, R. Tokala, D. M. Bajaj, N. Nagesh, K. K. Bokara, G. Kiranmai, U. J. Lakshmi, S. Vadlamani, V. Talla, N. Shankaraiah, Design and synthesis of substituted dihydropyrimidinone derivatives as cytotoxic and tubulin polymerization inhibitors, Bioorg. Chem. 93 (2019) 103317; b) N. P. Kumar, P. Sharma, T. S. Reddy, S. Nekkanti, N. Shankaraiah, G. Lalita, S. S. Kumara, S. K. Bhargava, V. G. M. Naidu, A. Kamal, Synthesis of 2,3,6,7-tetramethoxy phenanthren-9-amine: An efficient precursor to access new 4-aza-2,3-dihydropyrido phenanthrenes as apoptosis inducing agents, Eur. J. Med. Chem. 127 (2017) 305-317; c) P. Sharma, K. R. Senwar, M. K. Jeengar, T. S. Reddy, V. G. M. Naidu, A. Kamal, N. Shankaraiah, H_2O-Mediated isatin spiro-epoxide ring opening with NaCN: Synthesis of novel 3-tetrazolylmethyl-3-hydroxy-oxindole hybrids and their anticancer evaluation, Eur. J. Med. Chem. 104 (2015) 11-24; d) S. Nekkanti, V. Pooladanda, M. Veldandi, R. Tokala, C. Godugu, N. Shankaraiah, Synthesis of 1,2,3-triazolo-fused-tetrahydro-*β*-carboline derivatives *via* 1,3-dipolar cycloaddition reaction: Cytotoxicity

evaluation and DNA-binding studies, ChemistrySelect 2 (2017) 7210-7221; e) R. Tokala, S. Thatikonda, U. S. Vanteddu, S. Sana, C Godugu, N. Shankaraiah, Design and synthesis of DNA-interactive *β*-carboline-oxindole hybrids as cytotoxic and apoptosis inducing agents, ChemMedChem 13 (2018) 1909-1922.

32. B. M. Savall, F. Chavez, K. Tays, P. J. Dunford, J. M. Cowden, M. D. Hack, R. L. Wolin, R. L. Thurmond, J. P. Edwards, Discovery and SAR of 6-Alkyl-2,4-diaminopyrimidines as Histamine H4 Receptor Antagonists, J. Med. Chem. 57 (2014) 2429-2439.

33. a) D. Gerlier, N. Thomasset. Use of MTT colorimetric assay to measure cell activation J. Immunol. Methods, 94 (1986) 57-63; b) V. G. Reddy, T. S. Reddy, S. H. Privér, Y. Bai, S. Mishra, D. Wlodkowic, N. Mirzadeh, S. Bhargava, Synthesis of gold (I) complexes containing cinnamide: *in vitro* evaluation of anticancer activity in 2d and 3d spheroidal models of melanoma and *in vivo* angiogenesis, Inorg. Chem. 58 (2019) 5988-5999.

34. K. Okamoto, M. Ikemori-Kawada, A. Jestel, K. von Konig, Y. Funahashi, T. Matsushima, A. Tsuruoka, A. Inoue, J. Matsui, Distinct binding mode of multikinase inhibitor lenvatinib revealed by biochemical characterization, ACS Med. Chem. Lett. 6 (2015) 89−94.

35. F. Cheng, W. Li, G. Liu, Y. Tang, In silico ADMET prediction: recent advances, current challenges and future trends, Curr. Top. Med. Chem. 13 (2013) 1273-1289.

36. a) A .Y. Shaw, C. Y. Chang, M . Y. Hsu, P. J. Lu, C. N. Yang, H. L. Chen, C. Lo, C. Shiau, M. Chern, Synthesis and structure-activity relationship study of 8-hydroxyquinoline-derived Mannich bases as anticancer agents, Eur. J. Med. Chem. 7 (2010) 2860-2867. b) R. Cao, X. Guan, B. Shi, Z. Y. Chen, Z. H. Ren, W. L. Peng, H. Song Design, synthesis and 3D-QSAR of β-carboline derivatives as potent antitumor agents, Eur. J. Med. Chem 6 (2010) 2503-2515.

37. a) Y. Kubota, H. K. Kleinman, G. R. Martin, T. J Lawley. Role of laminin and basement membrane in the morphological differentiation of human endothelial cells into capillary-like structures, J. Cell Biol., 107 (1988) 1589–1598; b) K. L. DeCicco-Skinner, G. H. Henry, C. Cataisson, T. Tabib, J. C. Gwilliam, N. J. Watson, E. M. Bullwinkle, L. Falkenburg, R. C. O'Neill, A. Morin, J. S. Wiest, Endothelial cell tube formation assay for the *in vitro* study of angiogenesis, J. Vis. Exp. 91 (2014) 51312.

38. T. S. Reddy, S. H. Privér, N. Mirzadeh, R. B. Luwor, V. G. Reddy, S. Ramesan, S. K. Bhargava, Antitumor and Antiangiogenic Properties of Gold (III) Complexes Containing Cycloaurated Triphenylphosphine Sulfide Ligands, Inorg. Chem. 59 (2020) 5662-5673.

39. a) D. R. Senger, C. A. Perruzzi, M. Streit, V. E. Koteliansky, A. R. de Fougerolles, M. Detmar, The alpha(1)beta(1) and alpha(2)beta(1) integrins provide critical support for vascular endothelial growth factor signaling, endothelial cell migration, and tumor angiogenesis, Am. J. Pathol. 160 (2002) 195-204; b) T. S. Reddy, D. Pooja, S. H. Privér R. B. Luwor N. Mirzadeh S. Ramesan S. Ramakrishna, S. Karri, M. Kuncha, S. K. Bhargava, Potent and selective cytotoxic and anti-inflammatory gold (III) compounds containing cyclometalated phosphine sulfide ligands, Chem. Eur. J. Chem., 25 (2019), 14089-14100.

40. a) H. Rafehi1, C. Orlowski1, G. T. Georgiadis, K. Ververis1, A. El-Osta, T. C. Karagiannis, Clonogenic Assay: Adherent Cells, J. Vis. Exp. 49 (2011) 2573; b) T. S. Reddy, H. Kulhari, V. G. Reddy, V. Bansal, A. Kamal, R. Shukla, Design, synthesis and biological evaluation of 1,3-diphenyl-1H-pyrazole derivatives containing benzimidazole skeleton as potential anticancer and apoptosis inducing agents, Eur. J. Med. Chem. 101 (2015) 790-805.

41. a) L. G. Rodriguez, X. Wu, J. L. Guan, Wound-healing assay, Methods Mol Biol. 294 (2005) 23-9; b) R. Tokala, S. Thatikonda, S. Sana, P. Regur, C. Godugu, N. Shankaraiah, Synthesis and *in vitro* cytotoxicity evaluation of β-carboline-linked 2,4-thiazolidinedione hybrids: Potential DNA intercalation and apoptosis inducing studies, New J. Chem. 42 (2018) 16226-16236; c) T. S. Reddy, H. Kulhari, V. G. Reddy, A. V. S. Rao, V. Bansal, A. Kamal, R. Shukla, Synthesis and biological evaluation of pyrazolo-triazole hybrids as cytotoxic and apoptosis inducing agents, Org. Biomol. Chem. 13 (2015) 10136-10149.

42. a) J.-A. Choi, J.-Y. Kim, J.-Y. Lee, C.-M. Kang, H.-J. Kwon, Y.-D. Yoo, T.-W. Kim, Y.-S. Lee, S.-J. Lee, Induction of cell cycle arrest and apoptosis in human breast cancer cells by quercetin, Int. J. Oncol. 19 (2001) 837-844; b) W. Hu, J.J. Kavanagh, Anticancer therapy targeting the apoptotic pathway, Lancet Oncol. 4 (2003) 721-729. c) C, Jadala, M. Sathish, T. S. Reddy, V. G. Reddy, R. Tokala, S. K. Bhargava, N. Shankaraiaha, N. Nagesh, A. Kamal, Bioorg. Med. Chem. 27 (2019) 3285-3298.

43. a) I. Vermes, C. Haanen, H. Steffens-Nakken, C. Reutellingsperger, A novel assay for apoptosis flow cytometric detection of phosphatidylserine expression on early apoptotic

cells using fluorescein labelled annexin V, J. Immunol. Methods 184 (1995) 39-51; b) V. G. Reddy, T. S. Reddy, V. L. Nayak, B. Prasad, A. P. Reddy, A. Ravikumar, S. Taj, A. Kamal, Design, synthesis and biological evaluation of *N*-((1-benzyl-1*H*-1,2,3-triazol-4-yl)methyl)-1,3-diphenyl-1*H*-pyrazole-4-carboxamides as CDK1/Cdc2 inhibitors, Eur. J. Med. Chem. 122 (2016) 164-177.

44. a) M. Reers, S. T. Smiley, C. Mottola-Hartshorn, A. Chen, M. Lin, L. B. Chen, Mitochondrial membrane potential monitored by JC-1 dye, Methods Enzymol. 260 (1995) 406-417; b) V. G. Reddy, S. R. Bonam, T. S. Reddy, R. Akunuri, V. G. M. Naidu, V. L. Nayak, S.K. Bhargava, H. M. S. Kumar, P. Srihari, A. Kamal, 4β-amidotriazole linked podophyllotoxin congeners: DNA topoisomerase-IIα inhibition and potential anticancer agents for prostate cancer, Eur. J. Med. Chem. 144 (2018) 595-611.

45. a) J. M. Suski, M. Lebiedzinska, M. Bonora, P. Pinton, J. Duszynski, M. R. Wieckowski, Relation between mitochondrial membrane potential and ROS formation, Methods Mol. Biol. 1782 (2018) 357-381; b) T. S. Reddy, V. G. Reddy, H. Kulhari, R. Shukla, A. Kamal, V. Bansal, Synthesis of (*Z*)-1-(1,3-diphenyl-1H-pyrazol-4-yl)-3-(phenylamino)prop-2-en-1-one derivatives as potential anticancer and apoptosis inducing agents, Eur. J. Med. Chem. 117 (2016) 157-166.

46. a) M. A. Aziz, R. A. T. Serya, D. S. Lasheen, A. K. A. Aziz, A. Esmat, A. M. Mansour, A. N. B. Singab, K. A. M. Abouzid, Discovery of potent VEGFR-2 inhibitors based on furopyrimidine and thienopyrimidne scaffolds as cancer targeting agents, Sci. Rep. 6 (2016) 24460; b) V. G. Reddy, T. S. Reddy, C. Jadala, M. S. Reddy, F. Sultana, R. Akunuri, S. K. Bhargava, D. Wlodkowic, P. Srihari, A. Kamal, Pyrazolo-benzothiazole hybrids: Synthesis, anticancer properties and evaluation of antiangiogenic activity using in vitro VEGFR-2 kinase and in vivo transgenic zebrafish model, Eur. J. Med. Chem. 182 (2019) 111609.

47. Y. Wang, S. Wan, Z. Li, Y. Fu, G. Wang, J. Zhang, X. Wu, Design, synthesis, biological evaluation and molecular modeling of novel 1*H*-pyrazolo[3,4-*d*] pyrimidine derivatives as BRAFV600E and VEGFR-2 dual inhibitors, Eur. J. Med. Chem. 155 (2018) 210-228.

48. K. M. Elokely, R. J. Doerksen, Docking challenge: Protein sampling and molecular docking performance, J. Chem. Inf. Model. 53 (2013) 1934-1945.

Tables/Figures/Scheme captions

Table 1. IC_{50} (μM) values[a] against human cancer cell lines of carbamide derivatives **12a**–**aa** by MTT assay.

Table 2. The kinase inhibitory activities of the synthesized carbamide derivatives **12a**–**aa**

Table 3. Docking scores, H-bond interactions for some of the potent carbamide derived pyrimidine-thioindole conjugates and co-crystallized ligand

Table 4. ADME/T profile of some of the carbamide derived pyrimidine-thioindole conjugates and other known VEGFR-2 inhibitor

Table 5. PLS statistics of Field and Atom based 3D-QSAR models.

Table 6 Experimental and predicted pIC_{50} values against VEGFR-2 of compounds for Field and Atom-based 3D-QSAR models

Figure 1. Structures of carbamide, pyrimidine and indole centered VEGFR inhibitors **A**–**G**.

Figure 2. Design of carbamide derivatives of pyrimidine-thioindole conjugates.

Figure 3. a) Docking model represent the superimposition of **8** potential ligands and sorafenib; b & c) **12e** and **12k** ligand interactions in the binding site of VEGFR-2/KDR domain (PDB ID: 3WZE). The pink dashed lines represent hydrogen bonds. The potential ligands were shown as ball and stick model, while the interacting amino acids were denoted as thin tubes; **12e** was represented in green and **12k** in pink ball and stick model in the white background.

Figure 4. a) Poses represent the superimposition of potential ligands **12e** and **12k**; b) Poses represent the superimposition of potential ligands **12k** and sorafenib at VEGFR-2 kinase domain with possible interactions: The potential ligands were shown as ball and stick model, while the interacting amino acids were denoted as thin tubes and the sorafenib as was shown as violet ball and stick model in the white and black backgrounds.

Figure 5. Calculated pIC_{50} (Activity) versus experimental pIC_{50} (Predicted activity) values for the titled compounds obtained by PLS analysis using Field (**Figure 9A**) and Atom (**Figure 9B**) based models.

Figure 6. Field-based contour maps of compound **12e** (**A**, **B** and **C**) and **12p** (**D**, **E** and **F**). (**A**, **D**: All the contours; **B**, **E**: steric, electrostatic and hydrophobic contours; **C**, **F**: H-Bond donor and acceptor contours. Field steric contours: the green contours indicate the areas that are conducive to steric interaction; Field electrostatic contours: the blue contours indicate the regions that are favorable to the positively charged groups, the red contours indicate the regions that are favorable to the negatively charged groups; Field hydrophobic contours: the yellow contours represent regions where hydrophobic groups increase activity, while the white contours highlight regions that would favor hydrophilic groups; Field hydrogen bond donor and acceptor contours: the cyan and the blue-violet contours represent favorable and unfavorable hydrogen bond donor regions, respectively. The magenta and the gray contours represent favorable and unfavorable hydrogen bond acceptor regions, respectively.)

Figure 7. Atom-based cubic maps of compound **12e** and **12p**. (Electron withdrawing contours: the pale red cubes indicate the areas that are conducive to favorable electron withdrawing interaction, light-green cubes disfavorable electron withdrawing interaction; Atom hydrophobic contours: the orange-yellow cubes represent regions where hydrophobic groups increase activity, while the pink cubes highlight regions that would favor hydrophilic groups.

Figure 8. Structure activity relationship (SAR) of carbamide derivatives of pyrimidine-thioindole conjugates.

Figure 9. HUVECs capillary tube formation assay. Effect of compound **12k** (b & c) and reference drug sorafenib (d & e) on HUVEC cells at 2.5 and 5 μM concentrations.

Figure 10. Transwell migration assay. Effect of compound **12k** (b & c) and reference drug sorafenib (d & e) on HUVEC cells at 2.5 and 5 μM concentrations, which are invaded through the Matrigel-coated chamber, were stained with 0.25 % Crystal Violet. The photographs were taken by using an inverted microscope.

Figure 11. Colony formation inhibition effect of compound **12k** on MDA-MB-231 cells at 1, 3 and 5 μM, respectively.

Figure 12. Effect of compound **12k** on MDA-MB-231 cell migration. The cells were cultured in the absence and presence of compound **12k** (b & c) and sorafenib (d & e). The wounds were created in confluent monolayers of MDA-MB-231 with sterile micro pipette tip.

Figure 13. Apoptosis induced by compound **12e** (b & c) and **12k** (d & e) in MDA-MB-231 cells, observed by fluorescence microscopy using Hoechst 33242 staining after 48 h incubation with the compound. The cells were assessed for morphological changes, such as chromatin condensation and nuclear fragmentation, which are hallmarks of cell apoptosis.

Figure 14. Analysis of apoptotic cells induced by compound **12k** by flow cytometry. MDA-MB-231 cells exposed to increasing concentrations of compound **12k** (2.5 and 5 μM) were stained with Annexin V-FITC and PI. (LL: live; LR: early apoptotic; UR: late apoptotic; UL: necrotic).

Figure 15. Compounds **12e** and **12k** disrupted mitochondrial membrane integrity. MDA-MB-231 cells were treated with 2.5 and 5 μM concentrations of compound **12e** (b & c) and **12k** (d & e) for 48 h, stained with JC-1 and imaged by fluorescence microscopy. Scale bar represents 25 μm.

Figure 16. Compounds **12e** and **12k** induced production of intracellular ROS in MDA-MB-231 cancer cells. Cells were treated with increasing concentrations of compounds **12e** (b & c) and **12k** (d & e) for 48 h and stained with 10 μM of Carboxy-H_2DCFDA. The intensity of the green fluorescence due to the production of ROS was analyzed by flow cytometry.

Scheme 1. Synthesis of 1-(4-((1*H*-indol-3-yl)thio)-6-(amino)pyrimidin-2-yl)-3-phenylurea derivatives **12a**–**aa**.

Tables/Figures/Schemes

Table 1. IC_{50} (μM) values[a] against human cancer cell lines of carbamide derivatives **12a–aa** by MTT assay.

Entry	A549[b]	PC-3[c]	MDAMB-231[d]	HepG2[e]
12a	26.12 ± 2.12	14.13 ± 1.81	12.14 ± 1.21	**7.14 ± 0.62**
12b	33.40 ± 5.16	12.46 ± 2.11	**7.94 ± 0.92**	10.26 ± 0.81
12c	21.83 ± 1.66	28.44 ± 3.01	**6.93 ± 0.51**	22.47 ± 1.27
12d	> 50	33.81 ± 2.51	**8.65 ± 0.62**	**8.26 ± 0.97**
12e	25.40 ± 3.54	> 50	**5.94 ± 0.81**	**6.44 ± 0.44**
12f	18.62 ± 1.44	42.54 ± 5.21	10.13 ± 1.21	14.81± 1.89
12g	13.47 ± 0.97	17.40 ± 2.11	**7.26 ± 1.12**	17.12 ± 1.11
12h	33.13 ± 2.68	12.13 ± 1.16	**8.13 ± 1.14**	20.86 ± 0.91
12i	21.24 ± 1.51	14.93 ± 0.92	**7.89 ± 0.69**	11.44 ± 1.22
12j	11.82 ± 0.96	21.48 ± 1.12	13.10 ± 0.92	20.26 ± 1.17
12k	**6.41 ± 0.81**	**10.42 ± 0.78**	**5.85 ± 0.71**	**7.87 ± 1.18**
12l	**8.93 ± 1.21**	12.86 ± 1.19	**9.44 ± 1.14**	**7.15 ± 0.95**
12m	> 50	26.43 ± 2.12	35.92 ± 1.43	14.40 ± 0.92
12n	30.25 ± 4.25	21.64 ± 1.55	19.51 ± 1.38	**8.93 ± 0.81**
12o	> 50	33.43 ± 2.86	28.42 ± 2.01	11.42 ± 1.61
12p	> 50	19.81 ± 1.32	34.70 ± 2.31	**7.64 ± 0.64**
12q	> 50	42.47 ± 3.31	10.22 ± 0.82	**8.16 ± 1.31**
12r	> 50	17.29 ± 0.92	18.96 ± 1.43	16.35 ± 1.23
12s	> 50	22.45 ± 1.42	22.13 ± 1.52	11.74 ± 1.61
12t	42.31 ± 3.16	16.73 ± 1.93	**8.92 ± 0.61**	21.42 ± 1.73
12u	31.49± 2.11	11.12 ± 0.98	14.61 ± 1.24	**9.74 ± 1.24**
12v	> 50	17.54 ± 1.21	**7.86 ± 1.11**	14.32 ± 1.97
12w	23.45 ± 3.17	18.45 ± 2.72	13.42 ± 0.93	14.90 ± 1.19
12x	> 50	41.86 ± 5.92	17.10 ± 1.45	**8.37 ± 0.58**
12y	> 50	11.64 ± 2.17	> 50	24.82 ± 3.11
12z	> 50	15.10 ± 0.93	**9.46 ± 1.21**	17.40 ± 2.02
12aa	48.43 ± 6.91	32..28 ± 4.11	**10.26 ± 1.46**	12.63 ± 0.93
Sorafenib[f]	**7.43 ± 0.81**	**9.77 ± 1.12**	**11.84 ± 1.25**	**5.78 ± 0.41**

[a] IC_{50} values are the concentrations (μM) that cause 50% inhibition of cancer cell growth. Data represent the average of three independent experiments performed in quadruplet.
[b]Human lung cancer cell line
[c]Human prostate cancer cell line
[d]Human breast cancer cell line
[e]Human liver cancer cell line
[f] Reference compound.

Table 2. The kinase inhibitory activities of the synthesized carbamide derivatives **12a–aa**

Entry	R^1	R^2	VEGFR-2/KDR[c]
12a	morpholino	Phenyl	1.21 ± 0.14
12b	morpholino	4-methoxy phenyl	1.92 ± 0.15
12c	morpholino	4-chloro phenyl	1.44 ± 0.21
12d	morpholino	2- methyl-4-chloro phenyl	**0.35 ± 0.11**
12e	piperidin-1-yl	2,5-dimethyl phenyl	**0.31 ± 0.07**
12f	piperidin-1-yl	4-chloro phenyl	1.82 ± 0.21
12g	piperidin-1-yl	4-methoxy phenyl	1.13 ± 0.24
12h	piperidin-1-yl	Phenyl	4.55 ± 0.32
12i	pyrrolidin-1-yl	Phenyl	3.23 ± 0.28
12j	pyrrolidin-1-yl	4-methoxy phenyl	2.61 ± 0.33
12k	pyrrolidin-1-yl,	4-chloro phenyl	**0.33 ± 0.04**
12l	pyrrolidin-1-yl	2- methyl-4-chloro phenyl	**0.43 ± 0.05**
12m	phenyl amino	Phenyl	2.74 ± 0.23
12n	4-(pyridin-2-yl)piperazin-1-yl	Phenyl	1.71 ± 0.21
12o	4-(pyridin-2-yl)piperazin-1-yl	4-methoxy phenyl	4.15 ± 0.34
12p	4-(pyridin-2-yl)piperazin-1-yl	2- methyl-4-chloro phenyl	**0.92 ± 0.11**
12q	4-benzylpiperazin-1-yl	Phenyl	**0.67 ± 0.08**
12r	4-benzylpiperazin-1-yl	2,5-dimethyl phenyl	2.14 ± 0.21
12s	4-benzylpiperazin-1-yl	2- methyl-4-chloro phenyl	4.86 ± 0.27
12t	4-benzylpiperazin-1-yl	4-methoxy phenyl	**0.84 ± 0.13**
12u	cyclopropylamino	2- methyl-4-chloro phenyl	**0.44 ± 0.07**
12v	cyclopropylamino	Phenyl	5.22 ± 0.42
12w	phenyl amino	2- methyl-4-chloro phenyl	1.33 ± 0.18
12x	phenyl amino	2,5-dimethyl phenyl	2.82 ± 0.31
12y	(3,5-dimethoxyphenyl)amino	3,5-dimethoxy phenyl	3.51 ± 0.34
12z	(3,5-dimethoxyphenyl)amino	4-methoxy phenyl	1.43 ± 0.21
12aa	(4-chloro-phenyl)amino	Phenyl	1.81 ± 0.16
Sorafenib[b]	-	-	0.21± 0.02

The kinase inhibition % at 10 µM are the average of two independent experiments, [b] Reference compound. All the values are expressed as Mean ± SEM in which each treatment was performed in triplicate wells.

Table 3. Docking scores, H-bond interactions for some of the potent carbamide derived pyrimidine-thioindole conjugates and co-crystallized ligand.

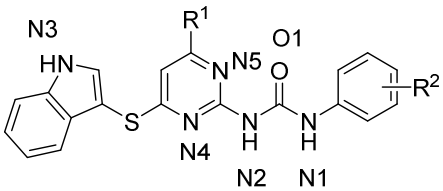

Carbamide derivatives

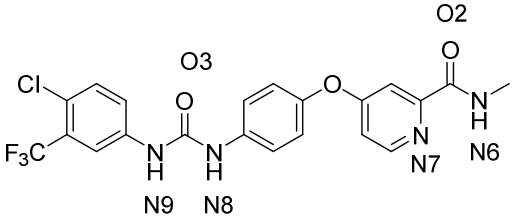

Sorafenib

Ligand ID	Docking Score	H-bond Interactions	
		Ligand	**Amino acid**
12d	-9.94	Lig@N1H, N2H Lig@O1	Glu885@OE1 Asp1046@NH
12e	-8.90	Lig@N1H, N2H Lig@O1	Glu885@OE1 Asp1046@NH
12k	-8.09	Lig@ N2H Lig@O1	Glu885@OE1 Asp1046@NH
12l	-10.15	Lig@N1H, N2H Lig@O1	Glu885@OE1 Asp1046@NH
12p	-8.97	Lig@N1H, N2H Lig@O1	Glu885@OE1 Asp1046@NH
12q	-8.21	Lig@ N2H Lig@O1	Glu885@OE1 Asp1046@NH
12t	-6.57	Lig@N1H Lig@O1	Glu815@OE2 Ile1025@NH
12u	-8.99	Lig@N1H, N2H Lig@O1	Glu885@OE1 Asp1046@NH
Sorafenib	-12.85	Lig@N6H, N7 Lig@N9H, N8H Lig@O3	Cys919@O2 Glu885@OE1 Asp1046@NH

Table 4. ADME/T profile of some of the carbamide derived pyrimidine-thioindole conjugates and other known VEGFR-2 inhibitor

Entry	Descriptors	Recommended values	Ligand ID								
			12d	**12e**	**12k**	**12l**	**12p**	**12q**	**12t**	**12u**	**sorafenib**
1	Molecular weight	130.0–725.0	494.998	472.607	464.971	478.998	571.098	535.665	595.718	464.971	464.831
2	Dipole moment	1.0–12.5	9.701	5.763	3.909	11.830	11.275	4.792	6.790	3.279	3.701
3	Total SASA	300–1000	770.541	797.546	801.495	888.418	734.108	854.278	791.748	929.237	9991.763
4	No. of rotatable bonds	0–15	5	6	4	4	4	4	4	6	8
5	Donor HB	0.0–6.0	3	4	3	3	3	3	3	3	3
6	Acceptor HB	2.0–20.0	6	4.5	4.5	6	6.2	4.5	4.5	6.5	8
7	QP Polarizability	13.0–70.0	49.268	55.160	50.616	51.795	61.530	62.789	66.014	49.256	49.764
8	QP logP o/w	2.0–6.5	4.391	5.659	5.169	5.468	6.222	5.634	5.761	4.857	4.105
9	QP log BB	−3.0 and 1.2	-0.488	-0.880	-0.713	-0.534	-0.795	-0.622	-0.806	-0.980	-0.994
10	Human Oral Absorption	1–3	3	1	1	1	1	1	1	1	1
11	Percent Human Oral Absorption	> 80% is high	100	100	93.336	100	84.988	73.789	73.865	100	95.846
12	Rule of Five violations	< 25% is low	0	1	1	1	2	2	2	0	0

Table 5. PLS statistics of Field and Atom based 3D-QSAR models

	$q^{2\,a}$	$r^{2\,c}$	$SE^{\,d}$	$F^{\,e}$	**Fraction**[f]				
					Steric	**Electrostatic**	**Hydrophobic**	**H-Donor**	**H-Acceptor**
Field 3D-QSAR	0.689	0.43	0.163	66.6	0.373	0.116	0.240	0.165	0.104
Atom 3D-QSAR	0.481	0.43	0. 179	71.2	-	0.007	0.698	0.050	-

[a] Cross-validated correlation coefficient;
[b] Optimum number of components obtained from cross-validated PLS analysis and same used in final non-cross-validated analysis;
[c] Non-cross-validated correlation coefficient;
[d] Standard error of estimate;
[e] F-test value. [f] Field contributions.

Table 6. Experimental and predicted pIC_{50} values against VEGFR-2 of compounds for Field and Atom-based 3D-QSAR models

Entry	pIC_{50} (experimental)	Field		Atom	
		pIC_{50} (predicted)	Prediction error	pIC_{50} (predicted)	Prediction error
12a	8.91	9.037	0.12	9.018	0.101
12b	8.72	8.972	0.256	8.682	-0.034
12c	8.84	8.714	-0.215	8.986	0.1467
12d	9.45	9.246	-0.204	8.740	-0.709
12e	9.50	9.186	-0.313	8.771	-0.728
12f	8.74	9.237	0.4977	9.047	0.3077
12g	8.95	8.986	0.036	8.693	-0.256
12h	8.31	8.648	0.3385	8.986	0.6767
12i	8.49	9.277	0.7873	9.093	0.6033
12j	8.58	8.927	0.3477	8.909	0.329
12k	9.48	9.307	-0.173	9.110	-0.369
12l	9.36	9.091	-0.268	9.007	-0.352
12m	8.56	8.626	0.0665	8.962	0.402
12n	8.76	8.579	-0.181	8.945	0.1858
12o	8.38	8.371	-0.0085	8.486	0.106
12p	9.03	9.013	-0.0165	8.711	-0.32
12q	9.17	8.859	-0.311	9.014	-0.155
12r	8.66	8.848	0.188	8.648	-0.012
12s	8.31	9.002	0.692	8.368	0.058
12t	9.05	8.782	-0.267	8.981	-0.069
12u	9.35	9.401	0.051	8.859	-0.490
12v	8.28	9.018	0.744	9.002	0.175
12w	8.87	9.011	0.142	8.797	-0.073
12x	8.55	8.402	-0.147	8.575	0.0253
12y	8.45	8.933	0.484	8.812	0.363
12z	8.84	8.983	0.144	8.765	-0.074
12aa	8.74	8.751	0.0114	8.732	-0.0078

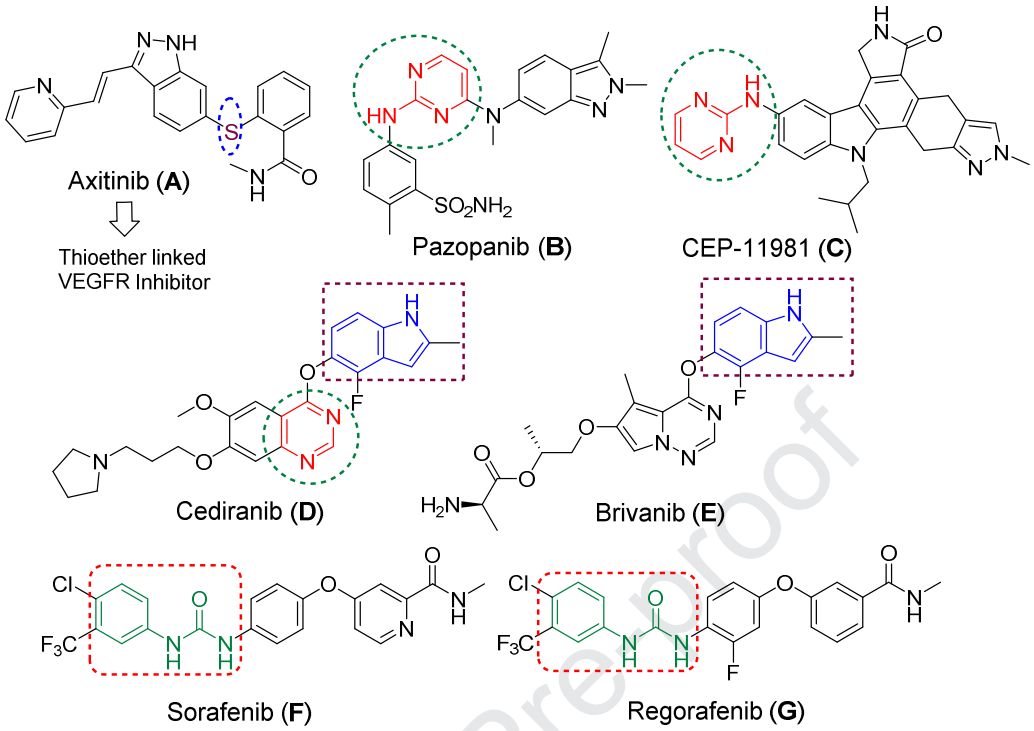

Figure 1. Structures of carbamide, pyrimidine and indole centered VEGFR inhibitors **A**–**G**.

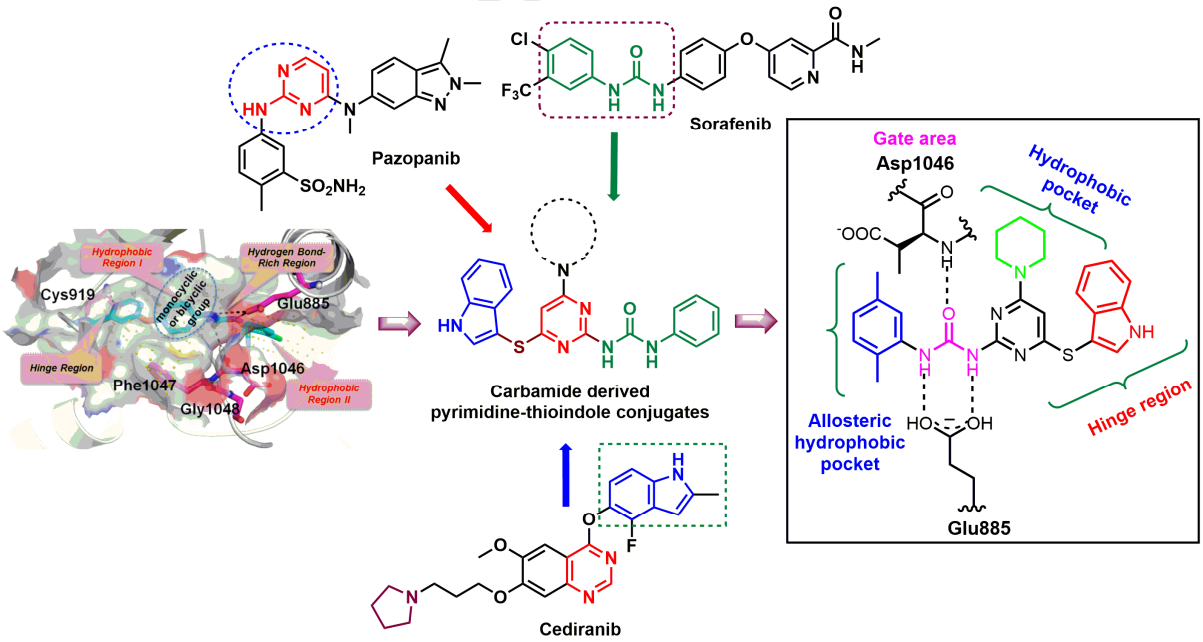

Figure 2. Design of carbamide derivatives of pyrimidine-thioindole conjugates.

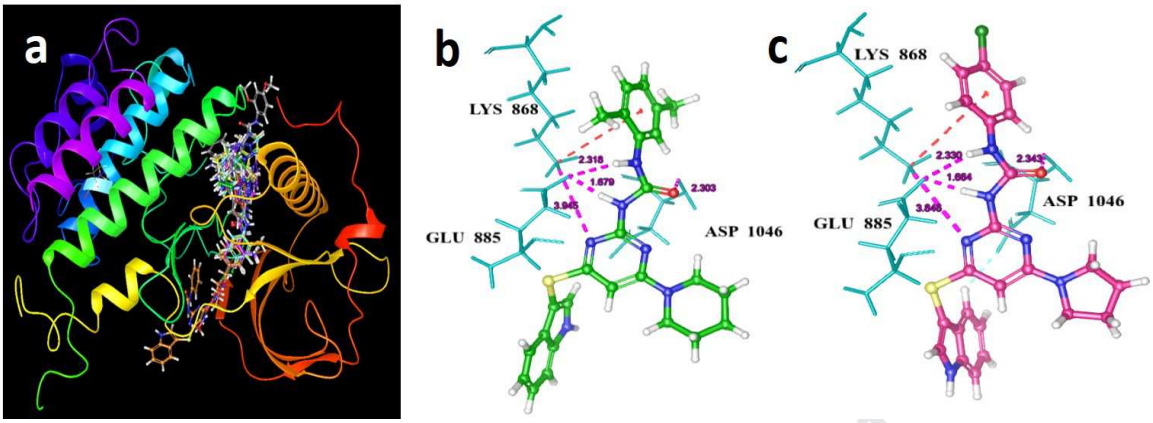

Figure 3. a) Docking model represent the superimposition of **8** potential ligands and sorafenib; b & c) **12e** and **12k** ligand interactions in the binding site of VEGFR-2/KDR domain (PDB ID: 3WZE). The pink dashed lines represent hydrogen bonds. The potential ligands were shown as ball and stick model, while the interacting amino acids were denoted as thin tubes; **12e** was represented in green and **12k** in pink ball and stick model in the white background.

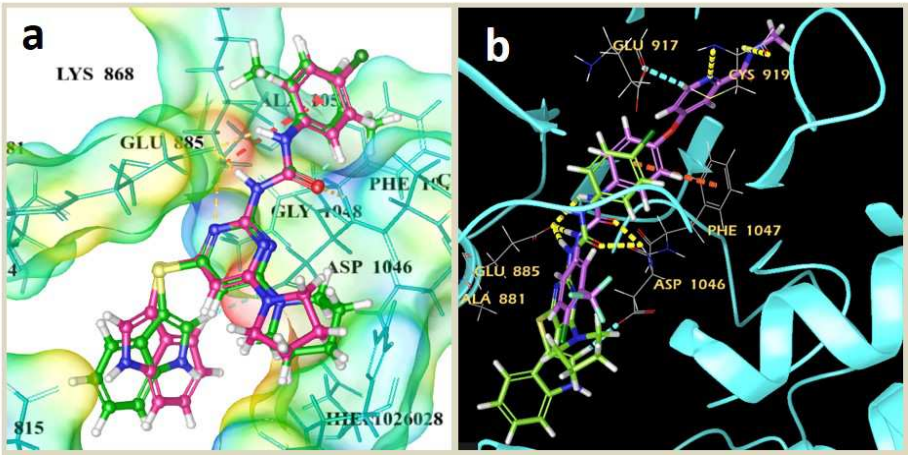

Figure 4. a) Poses represent the superimposition of potential ligands **12e** and **12k**; b) Poses represent the superimposition of potential ligands **12k** and sorafenib at VEGFR-2 kinase domain with possible interactions: The potential ligands were shown as ball and stick model, while the interacting amino acids were denoted as thin tubes and the sorafenib as was shown as violet ball and stick model in the white and black backgrounds.

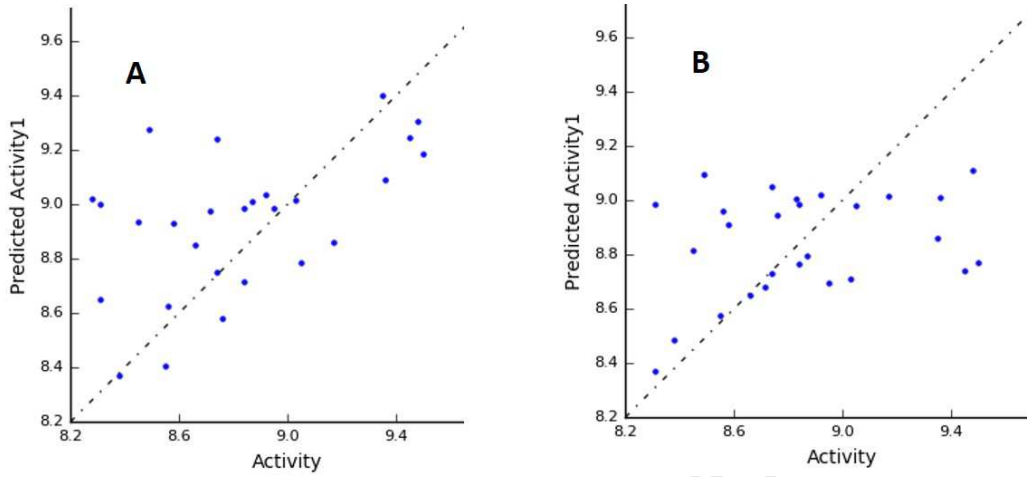

Figure 5. Calculated pIC_{50} (Activity) versus experimental pIC_{50} (Predicted activity) values for the titled compounds obtained by PLS analysis using Field (**Figure 9A**) and Atom (**Figure 9B**) based models.

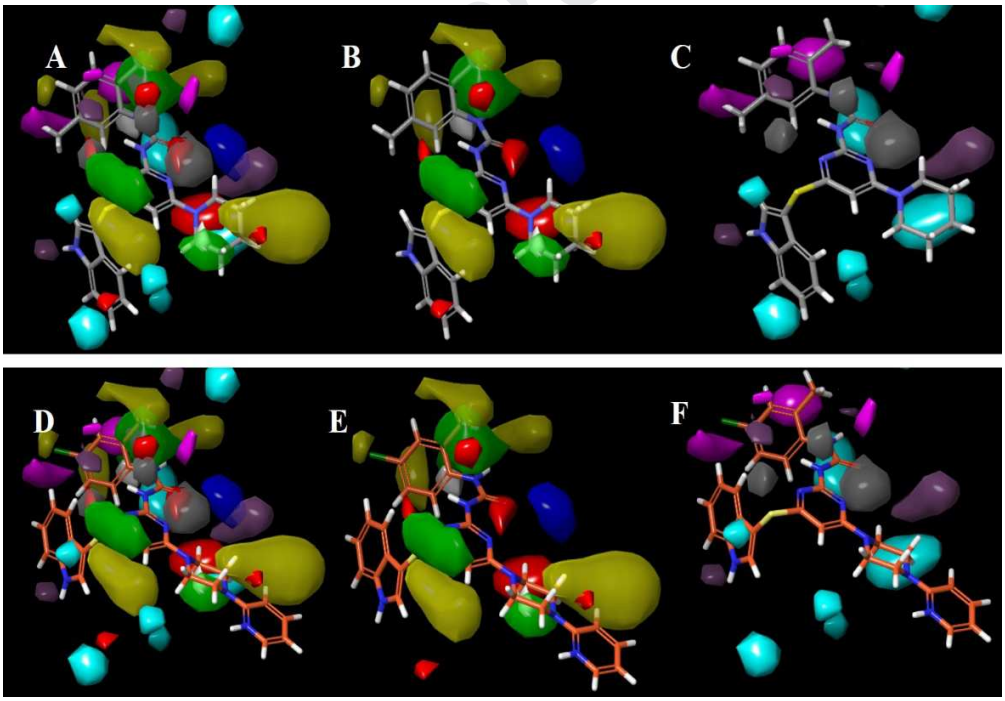

Figure 6. Field-based contour maps of compound **12e** (**A**, **B** and **C**) and **12p** (**D**, **E** and **F**). (**A**, **D**: All the contours; **B**, **E**: steric, electrostatic and hydrophobic contours; **C**, **F**: H-Bond donor and acceptor contours. Field steric contours: the green contours indicate the areas that are conducive to steric interaction; Field electrostatic contours: the blue contours indicate the regions

that are favorable to the positively charged groups, the red contours indicate the regions that are favorable to the negatively charged groups; Field hydrophobic contours: the yellow contours represent regions where hydrophobic groups increase activity, while the white contours highlight regions that would favor hydrophilic groups; Field hydrogen bond donor and acceptor contours: the cyan and the blue-violet contours represent favorable and unfavorable hydrogen bond donor regions, respectively. The magenta and the gray contours represent favorable and unfavorable hydrogen bond acceptor regions, respectively.)

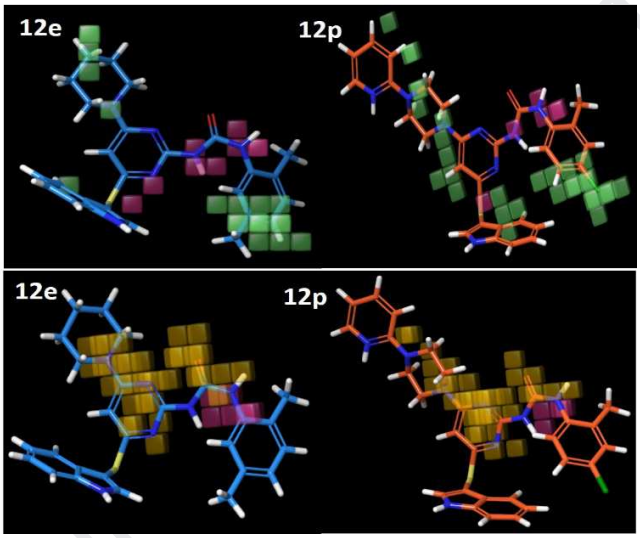

Figure 7. Atom-based cubic maps of compound **12e** and **12p**. (Electron withdrawing contours: the pale red cubes indicate the areas that are conducive to favorable electron withdrawing interaction, light-green cubes disfavorable electron withdrawing interaction; Atom hydrophobic contours: the orange-yellow cubes represent regions where hydrophobic groups increase activity, while the pink cubes highlight regions that would favor hydrophilic groups.

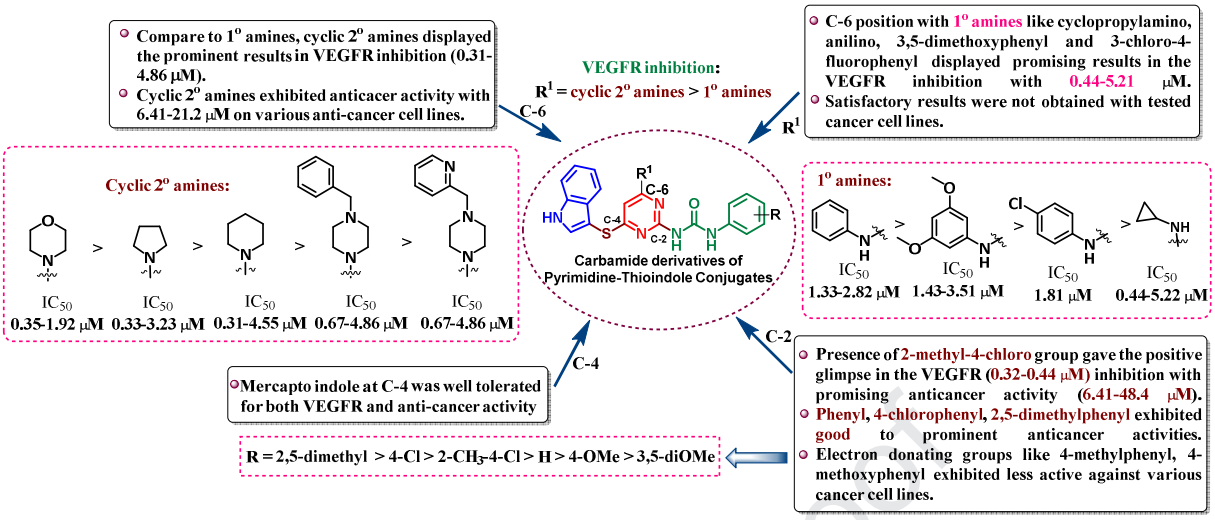

Figure 8. Structure activity relationship (SAR) of carbamide derivatives of pyrimidine-thioindole conjugates.

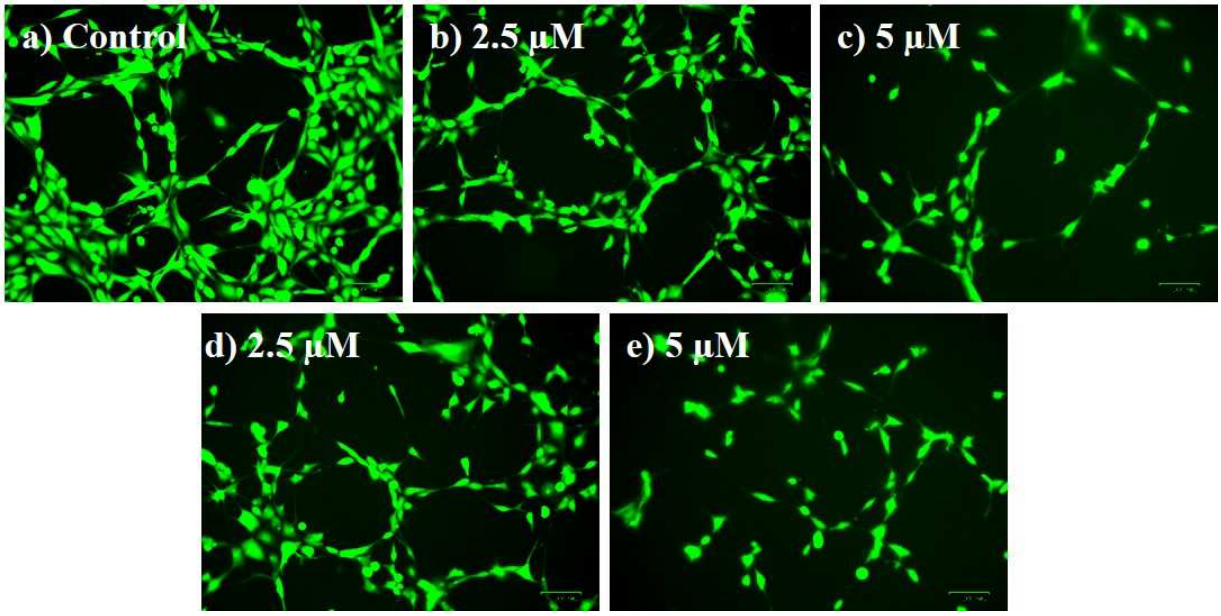

Figure 9. HUVECs capillary tube formation assay. Effect of compound **12k** (b & c) and reference drug sorafenib (d & e) on HUVEC cells at 2.5 and 5 µM concentrations.

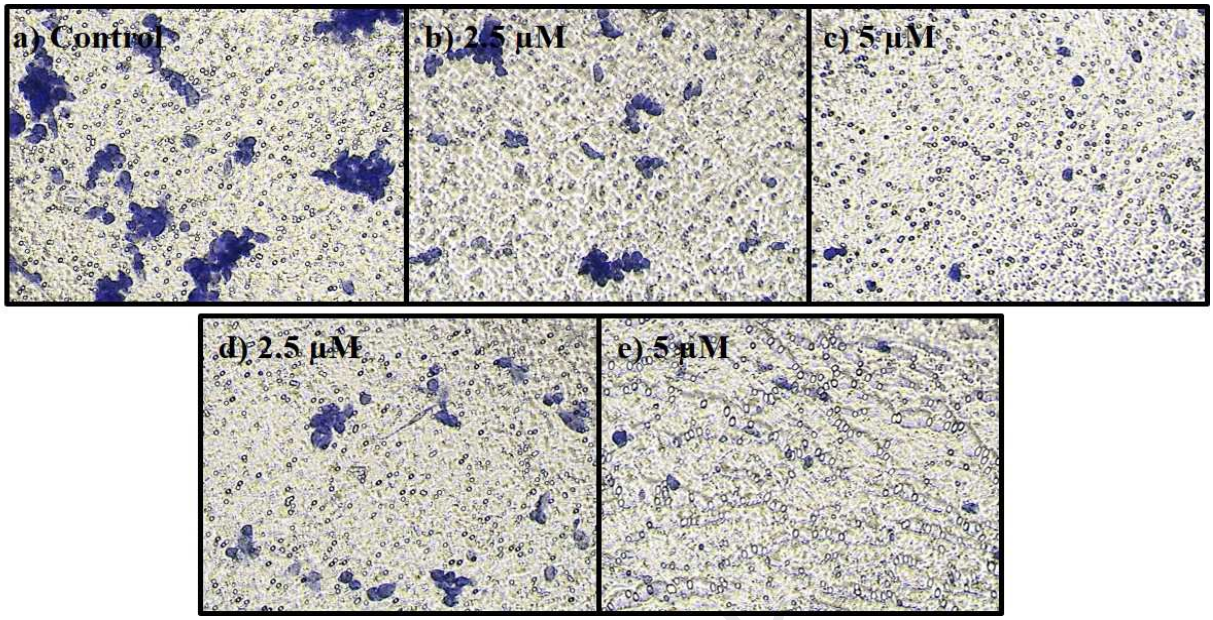

Figure 10. Transwell migration assay. Effect of compound **12k** (b & c) and reference drug sorafenib (d & e) on HUVEC cells at 2.5 and 5 µM concentrations, which are invaded through the Matrigel□coated chamber, were stained with 0.25 % Crystal Violet. The photographs were taken by using an inverted microscope.

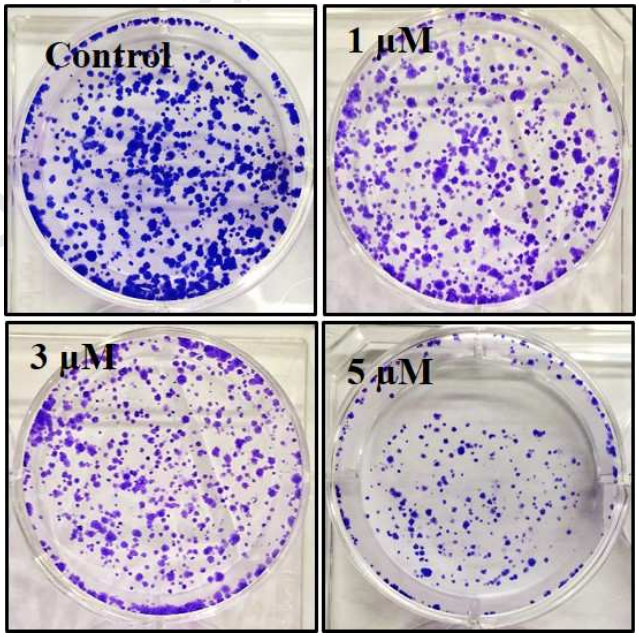

Figure 11. Colony formation inhibition effect of compound **12k** on MDA-MB-231 cells at 1, 3 and 5 µM, respectively.

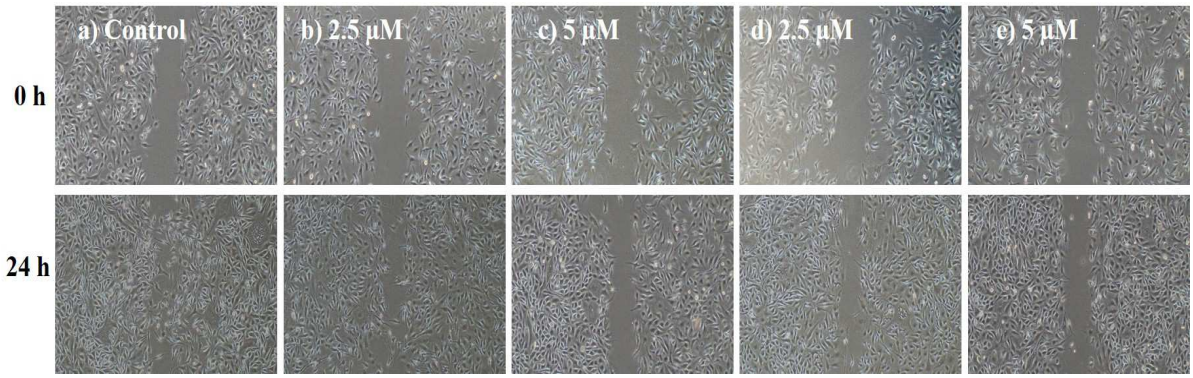

Figure 12. Effect of compound **12k** on MDA-MB-231 cell migration. The cells were cultured in the absence and presence of compound **12k** (b & c) and sorafenib (d & e). The wounds were created in confluent monolayers of MDA-MB-231 with sterile micro pipette tip.

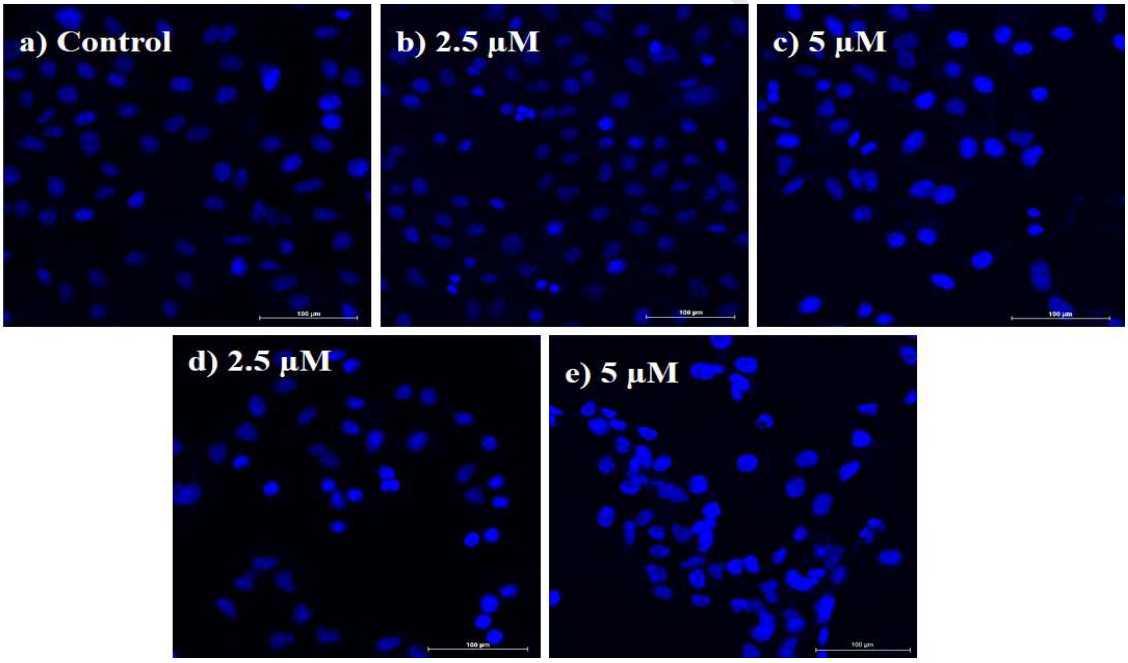

Figure 13. Apoptosis induced by compound **12e** (b & c) and **12k** (d & e) in MDA-MB-231 cells, observed by fluorescence microscopy using Hoechst 33242 staining after 48 h incubation with the compound. The cells were assessed for morphological changes, such as chromatin condensation and nuclear fragmentation, which are hallmarks of cell apoptosis.

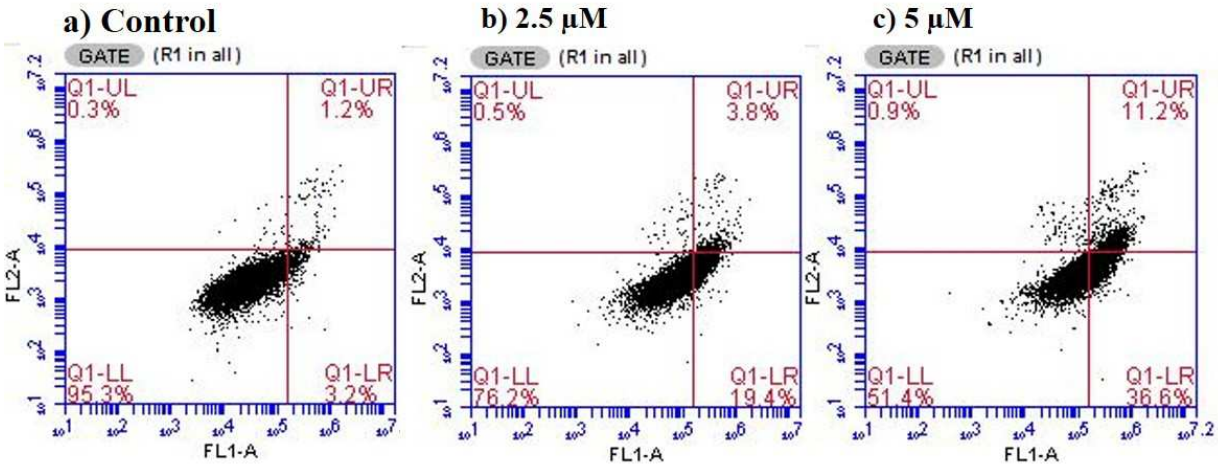

Figure 14. Analysis of apoptotic cells induced by compound **12k** by flow cytometry. MDA-MB-231 cells exposed to increasing concentrations of compound **12k** (2.5 and 5 µM) were stained with Annexin V-FITC and PI. (LL: live; LR: early apoptotic; UR: late apoptotic; UL: necrotic).

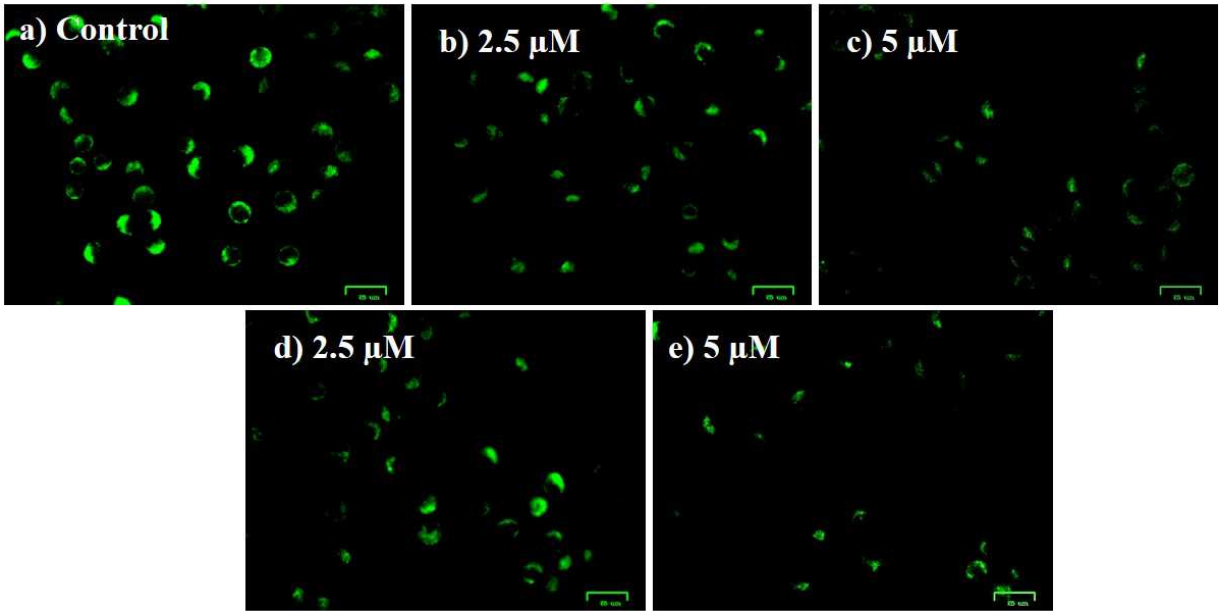

Figure 15. Compounds **12e** and **12k** disrupted mitochondrial membrane integrity. MDA-MB-231 cells were treated with 2.5 and 5 µM concentrations of compound **12e** (b & c) and **12k** (d & e) for 48 h, stained with JC-1 and imaged by fluorescence microscopy. Scale bar represents 25 µm.

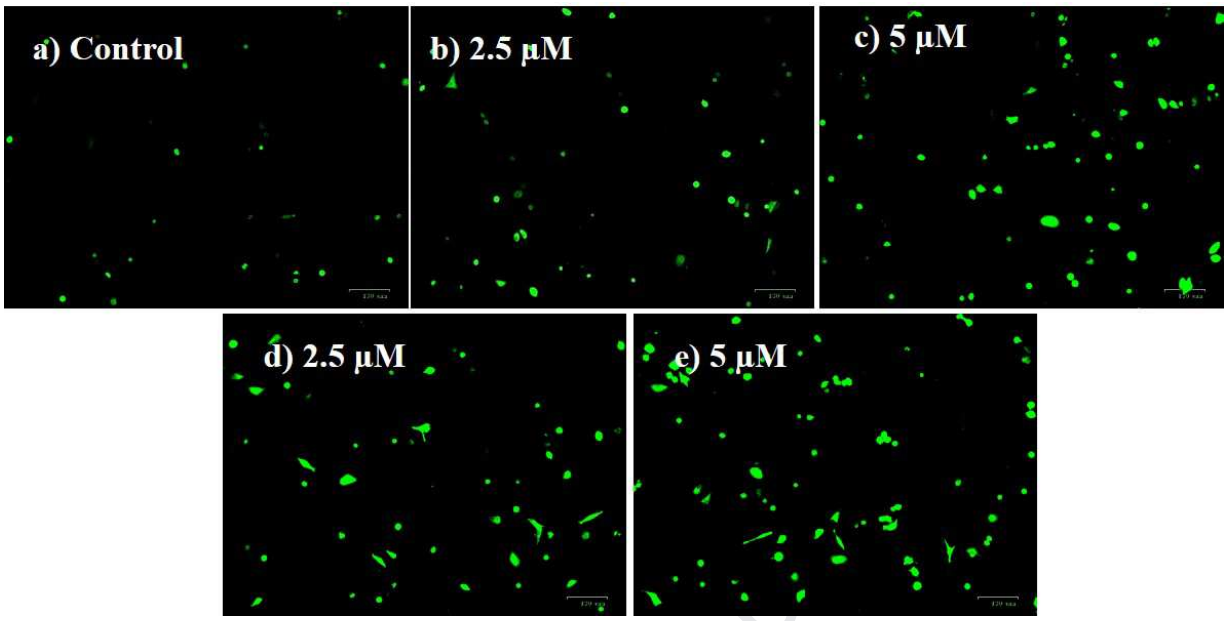

Figure 16. Compounds **12e** and **12k** induced production of intracellular ROS in MDA-MB-231 cancer cells. Cells were treated with increasing concentrations of compounds **12e** (b & c) and **12k** (d & e) for 48 h and stained with 10 µM of Carboxy-H_2DCFDA. The intensity of the green fluorescence due to the production of ROS was analyzed by flow cytometry.

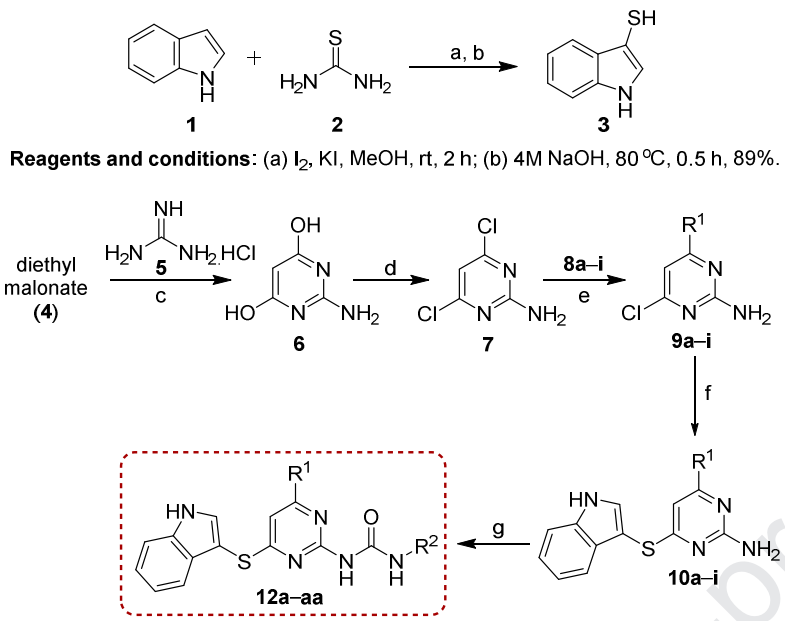

Reagents and conditions: (a) I_2, KI, MeOH, rt, 2 h; (b) 4M NaOH, 80 °C, 0.5 h, 89%.

Reagents and conditions: (c) NaOMe, MeOH, 70 °C, 5 h, 82%; (d) $POCl_3$, *N*,*N*-dimethyl aniline, 60 °C, 1 h, 79%; (e) R^1 = 1°/2° amines (**8a–i**); (**9a–c**) 1M HCl, 1,4-dioxane, 80 °C, 6-8 h, 60–85%; (**9d–g**) DIPEA, *n*-BuOH, 50–100 °C, 2–12 h, 75–90%, (**9h**) N_2, anhydrous DMF, Cs_2CO_3, 90 °C, 5 h, 89%; (**9i**) K_3PO_4,1,4-dioxane, 90 °C, 24 h, 85%; (f) **3**, KI, Et_3N, EtOH, reflux, 12–16 h, 65–88%; (g) R^2-NCO (**11a–f**), 1,4-dioxane, 100 °C, 3–8 h, 72–90%.

8a = phenyl amine
8b = (3,5-dimethoxyphenyl)amine
8c = (4-chloro-phenyl)amine
8d = morpholine
8e = piperidine
8f = pyrrolidine
8g = cyclopropylamine
8h = 4-benzylpiperazine
8i = 4-(pyridin-2-yl)piperazine

9a = **10a** = R^1 = phenyl amino
9b =**10b** = R^1 = (3,5-dimethoxyphenyl)amino
9c = **10c** = R^1 = (4-chloro-phenyl)amino
9d = **10d** = R^1 = morpholino
9e = **10e** = R^1 = piperidin-1-yl
9f = **10f** = R^1 = pyrrolidin-1-yl
9g = **10g** = R^1 = cyclopropylamino
9h = **10h** =R^1 = 4-benzylpiperazin-1-yl
9i = **10i** = R^1 = 4-(pyridin-2-yl)piperazin-1-yl

11a: R^2 = phenyl
11b: R^2 = 4-methoxy phenyl
11c: R^2 = 4-chloro phenyl
11d: R^2 = 2- methyl-4-chloro phenyl
11e: R^2= 2,5-dimethyl phenyl
11f: R^2= 3,5-dimethoxy phenyl

12a: R^1 = morpholino, R^2 = phenyl
12b: R^1 = morpholino, R^2 = 4-methoxy phenyl
12c: R^1 = morpholino, R^2 = 4-chloro phenyl
12d: R^1 = morpholino, R^2 = 2- methyl-4-chloro phenyl
12e: R^1 = piperidin-1-yl, R^2= 2,5-dimethyl phenyl
12f: R^1 = piperidin-1-yl, R^2 = 4-chloro phenyl
12g: R^1 = piperidin-1-yl, R^2 = 4-methoxy phenyl
12h: R^1 = piperidin-1-yl, R^2 = phenyl
12i: R^1 = pyrrolidin-1-yl, R^2 = phenyl
12j: R^1 = pyrrolidin-1-yl, R^2 = 4-methoxy phenyl
12k: R^1 = pyrrolidin-1-yl R^2 = 4-chloro phenyl
12l: R^1 = pyrrolidin-1-yl, R^2 = 2- methyl-4-chloro phenyl
12m: R^1 = phenyl amino, R^2 = phenyl
12n: R^1 = 4-(pyridin-2-yl)piperazin-1-yl, R^2 = phenyl
12o: R^1 =4-(pyridin-2-yl)piperazin-1-yl, R^2 = 4-methoxy phenyl
12p: R^1 = 4-(pyridin-2-yl)piperazin-1-yl, R^2 =2- methyl-4-chloro phenyl
12q: R^1 = 4-benzylpiperazin-1-yl, R^2 = phenyl
12r: R^1 = 4-benzylpiperazin-1-yl, R^2 = 2,5-dimethyl phenyl
12s: R^1 = 4-benzylpiperazin-1-yl, R^2 = 2- methyl-4-chloro phenyl
12t: R^1 = 4-benzylpiperazin-1-yl, R^2 = 4-methoxy phenyl
12u: R^1 = cyclopropylamino, R^2 = 2- methyl-4-chloro phenyl
12v: R^1 = cyclopropylamino, R^2 = phenyl
12w: R^1 = phenyl amino R^2 = 4-methyl phenyl
12x: R^1 = phenyl amino R^2 = 2- methyl-4-chloro phenyl
12y: R^1 = (3,5-dimethoxyphenyl)amino, R^2 = 3,5-dimethoxy phenyl
12z: R^1 = (3,5-dimethoxyphenyl)amino, R^2 = 4-methoxy phenyl
12aa: R^1 = (4-chloro-phenyl)amino, R^2 = phenyl

Scheme 1. Synthesis of 1-(4-((1*H*-indol-3-yl)thio)-6-(amino)pyrimidin-2-yl)-3-phenylurea derivatives **12a**–**aa**.

Research Highlights

- **27** pyrimidine-thioindoles (**12a-aa**) were designed using molecular hybridization approach.
- Inhibited VEGFR-2 protein with IC_{50} 0.31 ± 0.07 to 5.22 ± 0.42 µM values.
- 8 Compounds prominently suppressed VEGFR-2, with IC_{50} values of 310 to 920 nM.
- Angiogenesis inhibition was evident by HUVECstube formation assay.

Conflicts of interest

There are no conflicts of interest to declare